Domain Walls in the Z_2-symmetric Two Higgs Doublet Model

A thesis submitted to the University of Manchester for the degree of Master of Philosophy in the Faculty of Science and Engineering

2021

Kai Hong Law
Department of Physics and Astronomy

Contents

The total word count of the thesis is 11,923.

List of Figures

List of Tables

Abstract

This thesis first introduces topological defects in cosmology by explaining how they are formed by spontaneous symmetry breaking. Domain walls are then introduced in more detail, including a brief discussion of the domain wall problem in cosmology. The Standard Model (SM) of particle physics is then reviewed, with an explantation of the Higgs mechanism and the Goldstone bosons. After that, the shortcomings of the SM are briefly discussed, which pinpoint the necessity of physics beyond the SM. In particular, measurements of CP violation in particle physics are presented to motivate models beyond the SM such as supersymmetry. The Two Higgs Doublet Model (2HDM) is then introduced, with different parametrizations explained and masses of the physical scalars determined in terms of the parameters of the 2HDM. The remaining parts of the thesis rely on numerical simulations using the gradient flow technique. The theory of the technique is first introduced, before it is applied to the Z_2-symmetric 2HDM. In most of our original results, the Higgs doublets are parametrized as an electroweak rotation of the charge-violating vacua. The equations of motion are derived for the vacuum parameters and the Goldstone bosons. The equations are then solved using gradient flow, with the results presented in different parametrizations of the Higgs doublets. Local charge violation is observed in the solutions when G^2 is applied with asymmetric boundary conditions. CP-violating solutions are also seen for the Goldstone modes θ and G^3 respectively, when asymmetric boundary conditions are imposed.

Declaration

No portion of the work referred to in the thesis has been submitted in support of an application for another degree or qualification of this or any other university or other institute of learning.

Copyright Statement

DocID=24420), in any relevant Thesis restriction declarations deposited in the University Library, the University Library's regulations (see http://www.library.manchester.ac.uk/about/regulations/) and in the University's policy on Presentation of Theses.

Acknowledgements

I would like to thank my supervisor Professor Apostolos Pilaftsis for his guidance throughout my MPhil project. I have benefitted a lot from my discussions with him, and his attention to details has had a huge impact on my work.

I would also like to thank my parents for their continuous support during this very challenging year.

The Author

The author obtained his BSc in Physics and Theoretical Physics degree from Imperial College London in 2019. He then studied at the University of Cambridge, graduating with an MASt degree in Applied Mathematics in July 2020. He started to conduct research on Beyond the Standard Model physics as an MPhil student at the University of Manchester in September 2020. The results of his research are presented in this thesis.

Chapter 1

Introduction

The Standard Model (SM) of particle physics has been tested by many different experiments, and some of its predictions have been verified to a high degree of accuracy. Nevertheless, we believe that the SM is not complete since it is unable to explain some physical phenomena such as the matter-antimatter asymmetry in our universe. A myriad of models beyond the SM, which are extensions to the SM, have been proposed to account for these phenomena. One minimal extension is the Two Higgs Doublet Model (2HDM), which adds one more complex scalar doublet to the SM. It suggests the existence of five physical scalar particles, one of which is the SM Higgs boson that was first observed at the LHC in 2012.

There are several accidental symmetries that the 2HDM can acquire if we make certain parameter choices. The breaking of these symmetries can lead to topological defects in the model, such as domain walls, vortices and global monopoles. In this thesis, we will focus on one of the discrete symmetries – the Z_2 symmetry. Domain walls are formed when the Z_2 symmetry is broken during a phase transition of our universe. During symmetry breaking, regions in space that are causally disconnected can fall into different minima of the potential, hence domains are formed and the boundary surfaces between them are called domain walls.

In this thesis, we study the Z_2 domain walls in the 2HDM by first deriving the

equations of motion for the parameters in the Higgs doublets. We parametrize the Higgs doublets as an electroweak gauge rotation of the general vacua. The parameters of the rotation are the to-be Goldstone bosons. Numerical simulations are then performed to solve these equations using the gradient flow technique. Different boundary conditions are imposed for the Goldstone bosons, and the corresponding solutions are studied. We observe local charge violation when the Goldstone boson G^2 is applied with asymmetric boundary conditions.

The thesis will begin with an introduction of topological defects in Chapter 2. In particular, domain walls will be introduced, along with a brief discussion of the domain wall problem in cosmology. The SM will be reviewed in Chapter 3, with a discussion of the Higgs mechanism. Some open problems in the SM will also be discussed, which motivate the study of the 2HDM. CP violation will then be explained using measurements from particle physics experiments. In Chapter 4, the 2HDM is introduced. Different parametrizations of the Higgs doublets will be discussed, together with the mass matrices of the physical scalars. In Chapter 5, the gradient flow technique will first be discussed using ϕ^4 theory as an example. Then it is applied to the Z_2-symmetric 2HDM with CP-preserving vacua and charge-breaking vacua respectively. In Chapter 6, we consider the most general parametrization of the Higgs doublets using an electroweak gauge transformation of the charge-breaking vacua. We study the cases with only one Goldstone boson, solving the equations of motion in each case using gradient flow. Moreover, we investigate the cases with the generator of the U(1) symmetry $\theta(x)$ plus one other Goldstone boson. Finally, our results are summarized in Chapter 7.

Chapter 2

Topological Defects

Topological defects in cosmology are formed by spontaneous symmetry breaking, which is a well-known phenomenon in particle physics. More specifically, they are formed due to phase transitions in the early universe, when the temperature of the universe gradually decreases after the hot big bang. This process is called the Kibble mechanism. During cosmological phase transitions, when the temperature drops rapidly equilibrium can only be established locally, and so neighbouring regions which are causally disconnected will fall into different ground states, giving a stochastic distribution of defects [1]. The type of defects formed is determined by the topology of the vacuum manifold after the symmetry breaking, as suggested by Kibble in 1976 [2]. He introduced the idea that different types of topological defects such as domain walls, strings, monopoles and textures can be classified using homotopy theory.

There are many examples of topological defects in condensed matter systems that may sound more familiar to us than topological defects in cosmology. One of them is the domain of magnetic dipoles in ferromagnets. Inside a ferromagnet, each atom has a certain magnetic moment which interacts with the magnetic moments of other atoms. Below the Curie temperature, neighbouring magnetic dipoles in a region will align with one another to minimize the energy of the system. This results in domains of atoms with different magnetic orientations. Domain walls

exist at the boundaries of different domains, and they are topological defects of the system. When the temperature goes above the Curie temperature however, such domains will disappear because of thermal fluctuations. The formation of topological defects in cosmology is to some extent akin to the aforementioned process in ferromagnetism. When the temperature of the universe drops below some critical temperature, there would be spontaneous symmetry breaking which leads to the formation of topological defects, whereas above the critical temperature the symmetry would be restored and there would be no defects.

In particle physics, we can find topological defects in a theory by studying the symmetries and topologies of the vacuum manifold. Some of the first discoveries of topological defects in renormalizable field theories include the Nielsen-Olesen vortex line in the Higgs theory [3] and the 't Hooft-Polyakov monopole in the Yang-Mills theory [4].

Grand unified theories (GUTs), which attempt to unify the three fundamental forces described by the standard model, suggest that the known gauge symmetries in the standard model originate from a larger symmetry group G. This implies that the universe has experienced a series of phase transitions at which spontaneous symmetry breaking takes place. Through these transitions, the large symmetry group G is broken into smaller symmetry groups H_i, and eventually reduces into the residual symmetry group $\mathrm{SU}(3)_C \times \mathrm{U}(1)_{EM}$ that we see today after the electroweak symmetry breaking.

$$G \to H_1 \to H_2 \to ... \to \mathrm{SU}(3)_C \times \mathrm{SU}(2)_L \times \mathrm{U}(1)_Y \to \mathrm{SU}(3)_C \times \mathrm{U}(1)_{EM} \quad (2.1)$$

Topological defects can form at each of the phase transition, and whether this happens and the type of defects formed are determined by the topology of the vacuum manifold after each symmetry breaking. Topological defects can potentially have significant astrophysical effects on the evolution and the structure of the universe. If we do not observe a certain type of topological defect, we may be able to constrain or rule out some GUTs. This would be a good means of distinguishing between many different GUT models, complementary to the measurements from state-of-the-art particle physics experiments.

2.1 Spontaneous Symmetry Breaking

In a field theory with symmetry group G, spontaneous symmetry breaking occurs when the field ϕ obtains a non-zero vacuum expectation value (VEV) $\langle\phi\rangle = \phi_0 \neq 0$. The vacuum manifold is defined as

$$\mathcal{M} = \{\phi_0 : V(\phi_0) = V_{\min}\} \tag{2.2}$$

After the symmetry breaking $G \to H \subset G$, there is a residual symmetry group H. The action of H on an element of the vacuum manifold leaves the element invariant, so the residual symmetry group H is also called the stability group.

$$h\phi_0 = \phi_0, \quad \forall h \in H \tag{2.3}$$

We can map an element of the vacuum to another by a group element $g \in G$. We can assign equivalent classes $g_1 \sim g_2$ by considering the following:

$$\phi_0' = g_1\phi_0 = g_2\phi_0, \quad \phi_0, \phi_0' \in \mathcal{M} \tag{2.4}$$

We note that $g_2^{-1}g_1 \in H$. Therefore, we can express the vacuum manifold as a coset space:

$$\mathcal{M} \cong G/H \tag{2.5}$$

After the breaking of a continuous global symmetry $G \to H$, Goldstone theorem states that massless particles called Goldstone bosons will be formed for each generator of the broken symmetry [5]. The number of Goldstone bosons is given by

$$\text{Number of Goldstone bosons} = \dim(G/H) = \dim(G) - \dim(H) = \dim(\mathcal{M}) \tag{2.6}$$

2.2 Classification of Topological Defects

The topology of the vacuum manifold after spontaneous symmetry breaking determines whether there are any defects produced by the process. Homotopy theory can be used to study the topology of the vacuum manifold and to classify different types of topological defects. The n^{th} homotopy group of the vacuum manifold $\pi_n(\mathcal{M})$ classifies distinct mappings from the n-dimensional sphere S^n onto $\mathcal{M}$ which preserve the base point of the n-sphere. The classification of four different topological defects is shown in Table 2.1.

Topological defect	Dimension	Classification
Domain walls	2	$\pi_0(\mathcal{M}) \neq I$
Strings	1	$\pi_1(\mathcal{M} \neq I$
Monopoles	0	$\pi_2(\mathcal{M}) \neq I$
Textures	-	$\pi_3(\mathcal{M}) \neq I$

Table 2.1: Classification of topological defects using homotopy groups $\pi_n(\mathcal{M})$ [1].

In terms of the topology of the vacuum manifold $\mathcal{M}$, domain walls are formed when $\mathcal{M}$ contains disconnected components; strings are formed when $\mathcal{M}$ contains non-contractable loops (i.e. $\mathcal{M}$ is not simply connected); monopoles are formed when $\mathcal{M}$ contains non-contractible 2-spheres; and textures are formed when $\mathcal{M}$ contains non-contractible 3-spheres.

Domain walls are often formed by the spontaneous breaking of a discrete symmetry, since $\pi_0(Z_n)$ is non-trivial. In determining the nature of other topological defects, it is useful to use the property $\pi_n(S^n) \neq I$, where S^n is the n-dimensional sphere [6].

To justify the classification of domain walls using the homotopy group $\pi_0(\mathcal{M})$, we need to consider the mapping of the spatial infinities to the vacuum manifold. For a physical field configuration, we require the energy to be finite, hence we have to map the spatial infinities to the vacuum expectation values (VEVs) of the field. When the mapping is non-trivial, we can have different VEVs assigned to the spatial infinities, giving rise to a domain wall solution.

2.3 Domain Walls

Domain wall is the product of the spontaneous breaking of a discrete symmetry, which results in disconnected components in the vacuum manifold $\mathcal{M}$. These disconnected components are the different possible vacuum expectation values (VEVs) of the field ϕ. When the field undergoes such a phase transition, it will be required to make a choice of VEV. Since information cannot be communicated beyond the causal horizon, regions in space that are not in causal contact with each other may choose different VEVs. This leads to the formation of domains with different VEVs of the field. In order for the field to be smooth, it would interpolate continuously between the different VEVs in neighbouring regions. The region of interpolation is the two-dimensional domain wall separating the domains.

One of the simplest example of domain walls comes from the Goldstone model with a single scalar field and a double-well potential. The Lagrangian density of the theory is given by

$$\mathcal{L} = \frac{1}{2}(\partial_\mu \phi)(\partial^\mu \phi) - V(\phi) \tag{2.7}$$

where $V(\phi)$ is the following ϕ^4 potential:

$$V(\phi) = \frac{\lambda}{4}\left(\phi^2 - \eta^2\right)^2 \tag{2.8}$$

For simplicity, we will work with one spatial dimension and one time dimension. Note that the μ indices are contracted using the Minkowski metric $\eta_{\mu\nu}$, which is chosen to be $\mathrm{diag}(+1, -1)$. The Lagrangian is given by

$$L = \int_{-\infty}^{\infty} \mathcal{L}\, dx = \int_{-\infty}^{\infty} \left(\frac{1}{2}(\partial_\mu \phi)(\partial^\mu \phi) - V(\phi)\right) dx \tag{2.9}$$

The action is given by

$$S[\phi] = \int L\, dt = \int \mathcal{L}\, dx dt \tag{2.10}$$

We could derive the equation of motion for ϕ by varying ϕ in $S[\phi]$ and requiring

that $\frac{\delta S}{\delta \phi} = 0$. This would lead to the Klein-Gordon equation:

$$\partial_\mu \partial^\mu \phi + \frac{dV}{d\phi} = 0 \tag{2.11}$$

Since we are interested in a defect solution that is static, we can neglect the time derivative, and the equation of motion becomes

$$\frac{d^2\phi}{dx^2} = \lambda\phi\left(\phi^2 - \eta^2\right) \tag{2.12}$$

Note that the equation of motion in (2.12) is non-linear due to the ϕ^4 potential that we are considering. This non-linear equation gives rise to topological defects.

We should choose the parameter λ in the potential to be positive so that the potential is bounded from below. The potential is plotted in Figure 2.1(a). It is easy to see that the minima of the potential (or the vacua) are located at

$$\phi = \pm\eta \tag{2.13}$$

Note that the Lagrangian of the model in (2.7) is invariant under a Z_2 transformation $\phi \to -\phi$. After spontaneous symmetry breaking, the field would randomly choose one of the VEVs. The residual symmetry group is the trivial group **1**. The vacuum manifold in this case only contains the two disconnected vacua $\mathcal{M} = \{\eta, -\eta\}$, and $\mathcal{M} \cong Z_2$.

The solution to the equation of motion (2.12), which interpolates between the two vacua, is given by

$$\phi(x) = \eta \tanh\left(\sqrt{\frac{\lambda}{2}}\eta(x-a)\right), \tag{2.14}$$

where a is an arbitrary constant, which tells us the location of the kink. There is a myriad of solutions due to the translational invariance of the equation of motion. The kink solution with $a = 0$ is shown in Figure 2.1(b). If we swap the boundary conditions for ϕ at $\pm\infty$ and invert the kink, we would obtain another solution to the equation of motion, which is called the anti-kink. As mentioned at the beginning of the section, the region of interpolation represents a domain wall. Its

width is approximately given by

$$\delta \sim \left(\sqrt{\lambda}\eta\right)^{-1} \tag{2.15}$$

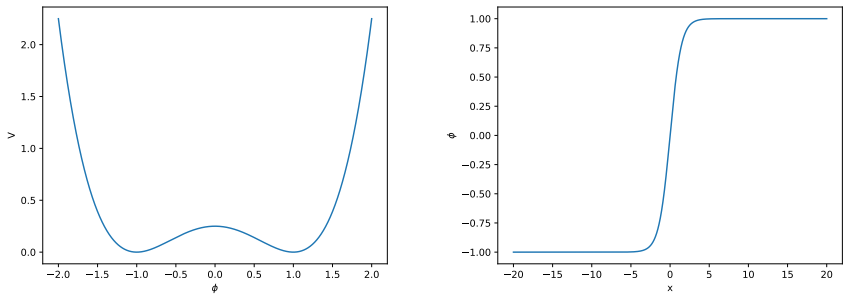

(a) The ϕ^4 potential $V(\phi)$ (b) The kink solution for $\phi(x)$

Figure 2.1: The 1+1 dimensional Goldstone model with the ϕ^4 potential $V(\phi) = \frac{\lambda}{4}(\phi^2 - \eta^2)^2$, showing the potential and the kink solution. The parameters are chosen to be $\lambda = 1$ and $\eta = 1\,\text{GeV}$.

For the static kink solution, the energy density is given by

$$\mathcal{E} = \frac{1}{2}\left(\frac{d\phi}{dx}\right)^2 + V(\phi) \tag{2.16}$$

Substituting the kink solution in (2.14) (with $a = 0$) into (2.16), we will obtain the following analytical expression for the energy density of the solution:

$$\mathcal{E} = \frac{1}{2}\lambda\eta^4 \text{sech}^4\left(\sqrt{\frac{\lambda}{2}}\eta x\right) \tag{2.17}$$

By integrating the energy density over space, we can find the energy per unit area of the domain wall:

$$E = \int_{-\infty}^{\infty} \mathcal{E}(x)\,dx = \frac{2\sqrt{2}}{3}\sqrt{\lambda}\eta^3 \tag{2.18}$$

2.4 The Domain Wall Problem in Cosmology

Domain walls are of our interest because they have great cosmological implications. Domain walls are formed by the breaking of discrete symmetries. In the early universe, these discrete symmetries should be restored since the temperatures were much higher than present. The universe then cools and undergoes a series of symmetry breaking phase transitions, where domain walls are formed. Subsequently, the energy density of the domain walls decreases as the universe expands. We can estimate the rate of decrease using a self-scaling argument. In chapters 5 and 6, we will show that the energy per unit area of a domain wall E can be obtained by solving the equations of motion of the system. Within a Hubble radius r, the total energy of the domain walls is proportional to Er^2. Then the energy density of the domain wall $\rho_{\rm dw}$, which is the energy per unit volume, follows the relation $\rho_{\rm dw} \propto Er^{-1}$. Since the horizon expands at the speed of light, we have $\rho_{\rm dw} \propto Et^{-1}$. Therefore, the energy density of domain walls scales as $(\text{time})^{-1}$. However, the energy densities of matter and radiation scale as $(\text{time})^{-2}$ in their respective epochs [7]. Consequently, domain walls would grow relative to matter and radiation, and eventually dominate the energy density of the universe. However, we do not currently observe any domain walls. This is known as the domain wall problem.

Requiring that domain wall domination occurs after the present day would impose constraints on particle models. In this thesis we will look into the Two Higgs Doublet Model (2HDM), which is one of the particle models beyond the Standard Model. In chapters 5 and 6, we will see that we can rescale the energy per unit area of the domain wall E by the Standard Model (SM) Higgs mass $M_h = 125\,\text{GeV}$ and the vacuum expectation value of the SM Higgs $v_{\rm SM} = 246\,\text{GeV}$. This results in the dimensionless energy $\hat{E} = \frac{E}{M_h v_{\rm SM}^2}$. Therefore, we can write the energy density of the domain wall as

$$\rho_{\rm dw} = A\hat{E} M_h v_{\rm SM}^2 t^{-1} \,, \tag{2.19}$$

where A is the number of domain walls per horizon. From the Friedmann equations, we can derive the following critical energy density that gives a flat universe

today:

$$\rho_{\text{crit}}(t_0) = \frac{3H_0^2 M_{\text{pl}}^2}{8\pi} \,, \tag{2.20}$$

where H_0 is the Hubble constant and M_{pl} is the Planck mass. We can then define the following dimensionless density parameter:

$$\Omega_{\text{dw}} = \frac{\rho_{\text{dw}}}{\rho_{\text{crit}}(t_0)} \tag{2.21}$$

In a similar manner, we can define density parameters for each of the other components of our universe, which are matter, radiation and dark energy. In order for our current universe to be flat (which is what we observe from measurements of the cosmic microwave background, supernovae and baryonic acoustic oscillations), we require $\sum_i \Omega_i = 1$. This means that we can impose the minimal constraint $\Omega_{\text{dw}} < 1$, which results in the limit

$$\frac{8\pi A \hat{E} M_h v_{\text{SM}}^2}{3H_0^2 t_0 M_{\text{pl}}^2} < 1 \tag{2.22}$$

In the context of the 2HDM, the energy of the domain wall solutions can be reduced by choosing a larger ratio between the two vacuum expectation values [8].

There are other methods to solve the domain wall problem. For example, if we make the discrete symmetries approximate, the domain walls would decay before domination occurs. By imposing the approximate symmetry, the potential will have a global minimum (the true vacuum), and a local minimum which has a higher energy (the false vacuum). This energy difference between the vacua would create a pressure on the domains of false vacuum, hence suppressing the domain walls at the boundaries [9].

Apart from imposing constraints on the model, the domain wall problem can also be solved if we introduce a period of inflation after the formation of domain walls. Inflation is a period of accelerated expansion of the universe. It was proposed to solve some of the problems in the big bang model such as the flatness problem and the horizon problem. Inflation can also be a cure for the domain wall problem – if domain walls were formed before inflation occurred, they would be inflated

beyond the current horizon and become unobservable [10, 11].

Chapter 3

The Standard Model of Particle Physics

Physicists have been studying the fundamental particles and forces of nature for a very long time. We used to think that atoms are the smallest constituents of matter, until J. J. Thomson discovered electrons in 1897, before Rutherford proposed the existence of the atomic nucleus in 1911. Since then there have been more discoveries of fundamental particles, and at the same time theorists like Dirac, Schwinger and Feymann started to formulate and explore Quantum Field Theory. Throughout the years the Standard Model was developed by applying quantum field theory and symmetries. The Standard Model has gone through many experimental verifications such as the confirmed predictions of the existence of the $W^{\pm}$ and Z^0 bosons at CERN in 1983 [12], and the discovery of the top quark at Fermilab in 1995 [13, 14]. The discovery of the Higgs boson in 2012 completed the Standard Model [15, 16].

The Standard Model is a self-consistent theory which describes all known elementary particles and their interactions using quantum field theory. These particles are classified into three families of leptons and quarks, as shown in Table 3.1. The first family of particles make up the matter that we know. The second and third families of particles are the heavier versions of the first family, and so they are

unstable and often will decay into the first family particles.

Quarks	$\begin{pmatrix} u \\ d \end{pmatrix}$	$\begin{pmatrix} c \\ s \end{pmatrix}$	$\begin{pmatrix} t \\ b \end{pmatrix}$
Leptons	$\begin{pmatrix} \nu_e \\ e \end{pmatrix}$	$\begin{pmatrix} \nu_\mu \\ \mu \end{pmatrix}$	$\begin{pmatrix} \nu_\tau \\ \tau \end{pmatrix}$

Table 3.1: Matter particles in the Standard Model. They are fermions with spin $\frac{1}{2}$, and are grouped into three different families.

The Standard Model describes all fundamental forces in nature except gravity. The three forces described by the Standard Model are encoded in the following gauge symmetry group:

$$G = \mathrm{SU}(3)_C \times \mathrm{SU}(2)_L \times \mathrm{U}(1)_Y \tag{3.1}$$

The $\mathrm{SU}(3)_C$ group describes the strong interactions which bind quarks into nucleons. The subscript C corresponds to colour and the strong force is mediated by eight massless gluons. The $\mathrm{SU}(2)_L$ group describes the weak interactions. The subscript L refers to left-handed to symbolize that weak interactions only involve left-handed particles. The subscript Y in $\mathrm{U}(1)_Y$ refers to hypercharge. The gauge group in equation (3.1) is broken by the Higgs mechanism, when the scalar field Φ obtains a non-zero vacuum expectation value (VEV). This mechanism will be discussed in more detail in the next section.

$$G \xrightarrow{\langle\Phi\rangle\neq 0} \mathrm{SU}(3)_C \times \mathrm{U}(1)_{EM} \tag{3.2}$$

The gauge bosons which correspond to the broken SU(2) group are the $W^\pm$ and Z^0 bosons. The $\mathrm{SU}(3)_C$ group is the symmetry group for Quantum Chromodynamics (QCD). The strong force binds quarks together with gluons to form colourless hadrons such as protons and neutrons. Therefore, quarks are confined except at high energies when the coupling strength decreases and the quarks gain asymptotic freedom. The subscript EM in the group $\mathrm{U}(1)_{EM}$ stands for electromagnetic, and it is the symmetry group for Quantum Electrodynamics (QED).

The spontaneously broken $\mathrm{SU}(2)_L \times \mathrm{U}(1)_Y$ gauge theory gives rise to both elec-

tromagnetic and weak interactions. This is known as the electroweak theory and the unification of the two interactions is one of the biggest achievements in physics [17, 18].

3.1 The Higgs Mechanism

The Higgs mechanism is used for explaining the origin of masses of the fermions and gauge bosons in the Standard Model. We first introduce a scalar field by adding a scalar potential to the Lagrangian. When the scalar field acquires a non-zero vacuum expectation value (VEV), i.e. the symmetry is spontaneously broken, quadratic terms of some gauge bosons would appear in the potential, which implies that the gauge bosons become massive. There would also be a quadratic term for a new scalar boson called the Higgs boson coming from the expansion around the vacuum, which means we would expect to see a massive Higgs boson. In 2012, the ATLAS and CMS experiments in CERN announced the discovery of the Higgs boson with a mass of about 125 GeV, which completed the last piece of the Standard Model [15, 16].

We will build up the gauge theory based on the group

$$G = \mathrm{SU}(2)_L \times \mathrm{U}(1)_Y \tag{3.3}$$

The gauge field for $\mathrm{SU}(2)_L$ is W^a_μ, with the field strength given by

$$W^a_{\mu\nu} = \partial_\mu W^a_\nu - \partial_\nu W^a_\mu - ig[W^a_\mu, W^a_\nu]\,, \tag{3.4}$$

where g is the gauge coupling of $\mathrm{SU}(2)_L$. The gauge field for $\mathrm{U}(1)_Y$ is B_μ, with the field strength given by

$$B_{\mu\nu} = \partial_\mu B_\nu - \partial_\nu B_\mu \tag{3.5}$$

The gauge coupling of $\mathrm{U}(1)_Y$ is labelled by g'.

We now introduce a complex scalar field Φ which is a $\mathrm{SU}(2)_L$ doublet with hypercharge $Y = \frac{1}{2}$. The bosonic part of the Lagrangian is then given by

$$\mathcal{L} = -\frac{1}{4}\big(W^a_{\mu\nu}\big)^2 - \frac{1}{4}B^2_{\mu\nu} + D_\mu\Phi(D^\mu\Phi)^\dagger - V(\Phi) \tag{3.6}$$

The covariant derivative of Φ is given by

$$D_\mu\Phi = \partial_\mu\Phi + igW^a_\mu T^a\Phi + \frac{i}{2}g'B_\mu\Phi\,, \tag{3.7}$$

where $T^a = \frac{\sigma^a}{2}$ are the generators of the $\mathrm{SU}(2)_L$ group. The scalar potential is given by

$$V(\Phi) = -\mu^2(\Phi^\dagger\Phi) + \lambda\big(\Phi^\dagger\Phi\big)^2 \tag{3.8}$$

The potential in (3.8) is the most general potential one can write down which is renormalizable and invariant under the action of $\mathrm{SU}(2)_L \times \mathrm{U}(1)_Y$. In order for the potential to be Hermitian, we require μ^2 and λ to be real. Also, for the potential to be convex and bounded from below, we need $\lambda > 0$.

Spontaneous symmetry breaking occurs when we choose $\mu^2 > 0$ and the field Φ obtain a non-zero VEV $v = \sqrt{\frac{\mu^2}{\lambda}}$:

$$\langle\Phi\rangle = \frac{1}{\sqrt{2}}\begin{pmatrix}0\\ v\end{pmatrix} \tag{3.9}$$

We can expand the field around the vacuum such that

$$\Phi = \frac{1}{\sqrt{2}}e^{-i\xi^a(x)T^a}\begin{pmatrix}0\\ v+h(x)\end{pmatrix}\,, \tag{3.10}$$

where $\xi^a(x)$ are the Goldstone bosons coming from the broken $\mathrm{SU}(2)_L$ group and $h(x)$ represents the Higgs boson. Substituting the field expansion in equation (3.10) back into the Lagrangian in equation (3.6), we would find that the Goldstone fields ξ^a can be absorbed into the gauge fields W^a_μ and B_μ. If we choose the unitary gauge, the fields ξ^a would become the longitudinal polarizations of the gauge bosons, hence giving them a mass. We can diagonalize the mass matrix by

using:

$$W_\mu^\pm = \frac{1}{\sqrt{2}}\left(W_\mu^1 \mp iW_\mu^2\right) \tag{3.11}$$

$$Z_\mu = W_\mu^3 \cos\theta_W - B_\mu \sin\theta_W \tag{3.12}$$

$$A_\mu = W_\mu^3 \sin\theta_W + B_\mu \cos\theta_W \tag{3.13}$$

θ_W is the Weinberg angle defined by

$$\tan\theta_W = \frac{g'}{g} \tag{3.14}$$

We can then identify the masses of the gauge bosons and the Higgs bosons to be

$$m_h = \sqrt{2\lambda}v\,, \quad m_{W_\mu^\pm} = \frac{vg}{2}\,, \quad m_{Z_\mu} = \frac{v}{2}\sqrt{g^2 + (g')^2} \tag{3.15}$$

There is no mass term for the field A_μ, which represents the photon in electromagnetism, so it has zero mass. This is due to the unbroken $\mathrm{U}(1)_{EM}$ group after the spontaneous symmetry breaking:

$$\mathrm{SU}(2)_L \times \mathrm{U}(1)_Y \xrightarrow{\langle\Phi\rangle\neq 0} \mathrm{U}(1)_{EM} \tag{3.16}$$

Even though the Goldstone theorem in (2.6) only applies to the breaking of global symmetries, it still predicts the correct number of Goldstone bosons in the case of electroweak symmetry breaking:

$$\text{No. of Goldstone bosons } \xi^a = \dim(\mathrm{SU}(2)_L \times \mathrm{U}(1)_Y) - \dim(\mathrm{U}(1)_{EM} = 3 \tag{3.17}$$

Using the homeomorphisms $\mathrm{SU}(2) \simeq S^3$ and $\mathrm{U}(1) \simeq S^1$, where S^n are the n-spheres, we can deduce that the vacuum manifold $\mathcal{M}$ satisfies the following relation:

$$\mathcal{M} \cong (\mathrm{SU}(2)_L \times \mathrm{U}(1)_Y)/\mathrm{U}(1)_{EM} \simeq (S'^3 \times S'^1)/S^1 \simeq S^3 \tag{3.18}$$

There is a non-trivial third homotopy group for the vacuum manifold, since $\pi_3[S^3] = Z$. From Table 2.1, we can see that the textures are formed as topological defects after the electroweak spontaneous symmetry breaking. Unlike the other defects, textures do not constitute any significant cosmological implications [19].

3.2 Beyond the Standard Model

Even though the Standard Model (SM) is a consistent theory which has survived many experimental tests, we believe that it is not complete as it cannot explain all the observations in physics. The SM only describes three of the four fundamental forces in nature, and has not yet been able to describe gravity. We are also unsure if the forces can be unified in some way at high energies. Furthermore, the SM fails to explain why there is more matter than antimatter in nature. This matter-antimatter asymmetry is needed to explain why we are made up of matter but not antimatter. The asymmetry can be accounted for by CP-violation in the Standard Model. However, CP-violation in the weak sector is not large enough to explain the asymmetry that we observe. CP-violation will be discussed in more detail in section 3.3.

On the cosmological front, the SM is unable to explain dark matter, which makes up about 20-25% of our universe. From rotation curves of galaxies, we observe that stars away from the galactic centre rotate faster than expected if only luminous matter is taken into account. We therefore believe there is some kind of matter which does not interact with light that causes the stars to move faster than expected. We need some theory beyond the SM to describe dark matter particles. Apart from dark matter, we also know very little about dark energy, which is responsible for the current acceleration of our universe.

Another open question in the SM is the hierarchy problem. In the SM, there are quantum loop corrections to the Higgs mass. If we use the Planck scale as the cut-off scale where quantum gravity effects become important, then the physical Higgs mass is about 15 orders of magnitude smaller than the Planck scale. This implies that an extreme fine tuning is required for the quantum correction of the Higgs mass to obtain the physical Higgs mass, which is known as the hierarchy problem.

Since there are still many things that we cannot explain using the SM, we believe that the SM is only an effective theory at low energies and it is not complete.

Many models beyond the SM have been proposed, one of which is supersymmetry (SuSy). In SuSy, for every fermion there is a "sfermion" which is a boson, and for every gauge boson there is a "gaugino" which is a fermion. SuSy can potentially solve the hierarchy problem in the SM, since the quantum loop corrections from fermionic loops to the Higgs mass can be cancelled by the corresponding bosonic loops.

SuSy also solves some other open problems in the SM. With SuSy, the running couplings of the symmetry groups of the SM join at some point at a scale close to the Planck scale. This would unify all three forces in the SM at some high energy scale, which is an improvement to the electro-weak unification. Furthermore, SuSy predicts at least twice the number of particles in the SM, some of which are called weakly interacting massive particles (WIMPs), which have the right properties to be dark matter particles. For example, the lightest neutralino in many SuSy models is a candidate for dark matter. Moreover, SuSy incorporates a lot of new mixing angles and phases into the model, which could potentially lead to more substantial CP-violating effects than the SM entails. This would help explain the matter-antimatter asymmetry in our universe.

Even though SuSy is an attractive model that could potentially answer some of the open questions in particle physics, so far no SuSy particle has been observed. This implies that SuSy particles cannot have the same mass as their SM counterparts, or else we would have already observed them in particle experiments. To explain the higher masses of the SuSy particles which are beyond the current reach of experiments, SuSy should be a broken symmetry. Since the scale of breaking is likely to be larger than the energy reached by current experiments, the argument that SuSy can solve the hierarchy problem is weakened, as the loop corrections from SuSy particles may no longer cancel the corrections from their SM counterparts.

One of the simpler SUSY theories is called the Minimal Supersymmetric Standard Model (MSSM). In this minimal supersymmetric extension to the SM, an additional Higgs doublet is introduced. One of the doublets is coupled to up-type quarks, the other to down-type quarks and charged leptons. The most general extension to the SM using two Higgs doublets is called the Two Higgs Doublet

Model (2HDM). This is an attractive model due to the relatively few additions of new parameters to the SM for explaining physics beyond the SM. There exist more complicated models, for example the N Higgs doublet models (NHDM), which contain more than two Higgs doublets [20]. Such models have more complicated mass terms and quartic couplings. In this thesis we will focus on the 2HDM, which will be discussed in more detail in chapter 4.

In the 2HDM, there are a total of eight degrees of freedom, four from each complex Higgs doublet. After the electroweak symmetry breaking, like in the SM, three of the degrees of freedom go to the masses of three electroweak gauge bosons. Unlike the SM, where there is only one Higgs boson, the 2HDM predicts a total of five physical Higgs bosons. There are a pair of charged Higgs ($H^{\pm}$), two neutral CP-even scalars (H^0, h^0), and one neutral CP-odd scalar (A^0). For the potential, instead of the two parameters in the SM Higgs potential, there are altogether fourteen parameters in the general 2HDM potential in order for the theory to be renormalizable.

In the general 2HDM, flavour changing neutral currents (FCNCs) are allowed, which lead to interactions in which the flavour of the fermion is changed but its charge remains the same. These currents appear in the model because the Yukawa couplings are not diagonalized after the diagonalization of the fermion mass matrices [21]. We know from experiments that these interactions are very rare, so we need some mechanisms to suppress the couplings between fermions of the same charge in the 2HDM. One way is to impose a discrete symmetry in one of the Higgs doublets, which would diagonalize the Yukawa couplings and suppress FCNCs. This motivates the study of discrete symmetries, such as the Z_2 symmetry, in the 2HDM.

3.3 C, P, T Symmetries

Symmetries are important in describing the nature. A symmetry is a transformation of dynamical variables that leaves the form of physical laws invariant. A simple

example would be the rotational symmetry in Newton's second law of motion - the law holds whichever set of coordinate axes we choose to use. From Noether's theorem, we know that every symmetry corresponds to a conserved quantity. For example, rotational symmetry in a system leads to a conserved angular momentum; translational symmetry leads to a conserved momentum; and time translation symmetry leads to a conserved energy. In particle physics, there are also important symmetries such as parity (P), charge conjugation (C) and time reversal (T). Parity is an operation that reflects a polar vector, such as the momentum vector, through the origin. Charge conjugation replaces a particle with its antiparticle, which has the opposite electric charge and other quantum numbers. Time reversal is similar to parity, but instead of reversing the spatial axes it reverses the time axis through the origin. The CPT theorem suggests that any Lorentz invariant, local and unitary quantum field theory should be invariant under the combination of C, P, and T transformations. It is difficult to study the T symmetry in particle interactions, since no particles are T eigenstates. We will see later that the combination of CP is violated in weak interactions. Therefore from the CPT theorem, we believe that T should also be violated in the weak sector. Below we will look briefly into the C, P and CP symmetries and how they are conserved or violated in different interactions.

It has been observed that the weak interaction does not obey C or P symmetries, while the strong the electromagnetic (EM) interactions do. An example of the conservation of the charge quantum number can be seen in the EM decay of the neutral pion π^0. From QED we know that it can decay either into two photons or three photons. Without considering the C symmetry, the three photon case would have a branching ratio of 1% because of the suppression by the coupling at the extra vertex. However, the three photon decay has never been observed because of charge violation. The neutral pion π^0 has a charge quantum number of $+1$ while the photon has a charge quantum number of -1. Comparing the charge quantum numbers for the two decay routes, we have $C_{\gamma\gamma} = +1$ and $C_{\gamma\gamma\gamma} = -1$. Since charge is conserved in an EM decay, the three photon decay is not allowed.

It is well known that weak interactions do not conserve C or P. The weak coupling

strength depends on the handedness of the fermions. In particular, weak bosons only interact with left-handed fermions and right-handed antifermions. In the limit that the velocity of the fermions $v \to c$, handedness corresponds to helicity, which is the projection of the spin onto its momentum. In this case weak bosons only interact with fermions with helicity $h = -\frac{1}{2}$ and antifermions with $h = +\frac{1}{2}$. We can see that this implies the violation of C and P symmetries by using the following example.

Consider an incoming neutrino (which is massless so has $v \approx c$) with helicity $h = -\frac{1}{2}$. Under a parity transformation, the momentum vector of the neutrino flips sign since it it a polar vector. The spin vector being an axial vector however, does not change sign. As a result, the helicity of the neutrino changes to $h = +\frac{1}{2}$. In the relativistic limit, this means that the neutrino becomes right-handed, which forbids them to be involved in any weak interactions. Therefore, weak interactions violate the P symmetry.

A similar consideration would show that weak interactions violate the C symmetry as well. If we apply a charge operation on the neutrino, it becomes an antineutrino, but the spin and momentum vectors remain unchanged. This means that we will get a left-handed antineutrino, which is forbidden in weak interactions.

We might naively think that weak interactions preserve the combined CP symmetry. For example, if we apply the parity operation and then the charge operation on a left-handed neutrino, we will get a right-handed antineutrino, which is allowed in weak interactions. However, experimental observation of the decays of K_L^0 and B^0 mesons indicates a small CP violating effect in weak interactions. The first observation of CP violation was made in 1964, when the decay modes of K_L^0 were studied [22]. The neutral kaon can decay either to a lepton or an antilepton:

$$K_L^0 \to l^+ + \nu_l + \pi^- \tag{3.19}$$

$$K_L^0 \to l^- + \bar{\nu}_l + \pi^+ \tag{3.20}$$

It was observed that the K_L^0 will decay more often to an l^+ rather than an l^-, which is a sign of CP violation.

In 2004, there was another observation of CP violation, which occurred in B^0 decays [23, 24]. The following two decays were studied:

$$B^0 \to K^+ + \pi^- \tag{3.21}$$

$$\bar{B}^0 \to K^- + \pi^+ \tag{3.22}$$

With equal numbers of B^0 and $\bar{B}^0$ at first, it was found that more $K^+\pi^-$ pairs were produced than $K^-\pi^+$ pairs. The asymmetry observed was larger than that observed in kaon decays.

More recently, the LHCb collaboration at CERN discovered CP violation in D^0 meson in 2019 by measuring the decay rates of D^0 and $\bar{D}^0$ [25]. The result was established at 5.3σ, and it agreed with the upper end of the expected range of CP violation in D^0 decays.

In October 2020, LHCb announced the first observation of time-dependent CP violation in B_S^0 decays [26]. Since B^0 and B_S^0 are not energy eigenstates, they oscillate into their antiparticles and back. This leads to a time-dependent CP violation in B^0 and B_S^0 decays. The observation of the effect was made at 6.7σ. The data was consistent with the observation of time-integrated CP violation in B_S^0 decays made in 2013. Further analysis is needed to determine whether the result would hint at any physics beyond the SM, in particular if it would contribute to an extra source of CP violation to explain the matter-antimatter asymmetry in our universe.

CP violation is necessary to explain why there is more matter than antimatter in our universe. Indeed it is one of the three Sakharov conditions that are required to explain the matter-antimatter asymmetry [27]: (i) baryon number violation; (ii) C and CP violation; (iii) thermal non-equilibrium. We have seen examples of CP violation in the weak sector that are predicted by the SM. However, the amount of CP violation in the SM is not enough to explain the matter-antimatter asymmetry in our universe. Hence we need models beyond the SM, for example SuSy, to provide extra sources of CP violation.

Chapter 4

The Two Higgs Doublet Model

In the Two Higgs Doublet Model (2HDM), there is an addition of a complex scalar doublet to the scalar sector in the Standard Model (SM) [28]. It predicts five physical scalars after spontaneous symmetry breaking: two neutral CP-even states (h^0 and H^0), one of which can be identified with the SM Higgs; a CP-odd neutral scalar (A^0); and two charged scalars ($H^{\pm}$). The other three degrees of freedom in the 2HDM go to the longitudinal components of the $W^{\pm}$ and Z^0 bosons via the Higgs mechanism, similar to the case in the SM. The 2HDM contains several accidental symmetries depending on the choices of parameters. The breaking of these symmetries could result in different topological defects such as domain walls, vortices and monopoles [30]. In this thesis, we will study domain walls in the 2HDM which are formed by the breaking of discrete symmetries. Numerical simulations will be performed to find solutions to the equations of motion of the system.

There are three accidental discrete symmetries Z_2 ($\Phi_{1(2)} \to \pm\Phi_{1(2)}$), CP1 ($\Phi_{1(2)} \to \Phi^*_{1(2)}$) and CP2 ($\Phi_{1(2)} \to -\Phi^*_{2(1)}$) in the 2HDM that give rise to domain wall solutions. In this thesis we will focus on the Z_2 symmetry. It belongs to a class of symmetries called the Higgs Family (HF) symmetries because it only involves the transformation of the two Higgs doublets $\Phi_{1,2}$ but not their complex conjugates.

The Lagrangian of the electroweak sector in the 2HDM is given by

$$\mathcal{L} = -\frac{1}{4}(W^a_{\mu\nu})^2 - \frac{1}{4}B^2_{\mu\nu} + D_\mu\Phi_1(D^\mu\Phi_1)^\dagger + D_\mu\Phi_2(D^\mu\Phi_2)^\dagger - V(\Phi_1,\Phi_2)\,, \tag{4.1}$$

where as in the SM $W_{\mu\nu}$ is the field strength for the gauge group $\mathrm{SU}(2)_L$:

$$W^a_{\mu\nu} = \partial_\mu W^a_\nu - \partial_\nu W^a_\mu - ig[W^a_\mu, W^a_\nu]\,, \tag{4.2}$$

and $B_{\mu\nu}$ is the field strength for $\mathrm{U}(1)_Y$:

$$B_{\mu\nu} = \partial_\mu B_\nu - \partial_\nu B_\mu \tag{4.3}$$

As a reminder, the covariant derivative is given by

$$D_\mu = \partial_\mu + \frac{i}{2}gW^a_\mu\sigma^a + \frac{i}{2}g'B_\mu\,, \tag{4.4}$$

where g and g' are the gauge couplings of $\mathrm{SU}(2)_L$ and $\mathrm{U}(1)_Y$ respectively.

The most general tree-level scalar potential of the 2HDM is given by [20, 32]

$$\begin{aligned} V(\Phi_1,\Phi_2) =& -\mu_1^2(\Phi_1^\dagger\Phi_1) - \mu_2^2(\Phi_2^\dagger\Phi_2) - [m_{12}^2(\Phi_1^\dagger\Phi_2) + \text{h.c.}] \\ &+ \lambda_1(\Phi_1^\dagger\Phi_1)^2 + \lambda_2(\Phi_2^\dagger\Phi_2)^2 + \lambda_3(\Phi_1^\dagger\Phi_1)(\Phi_2^\dagger\Phi_2) + \lambda_4(\Phi_1^\dagger\Phi_2)(\Phi_2^\dagger\Phi_1) \\ &+ \left[\frac{\lambda_5}{2}(\Phi_1^\dagger\Phi_2)^2 + \lambda_6(\Phi_1^\dagger\Phi_1)(\Phi_1^\dagger\Phi_2) + \lambda_7(\Phi_2^\dagger\Phi_2)(\Phi_1^\dagger\Phi_2) + \text{h.c.}\right] \end{aligned} \tag{4.5}$$

There are a total of 14 free parameters coming from $\mu_1^2, \mu_2^2, \lambda_1, \lambda_2, \lambda_3$ and λ_4, which are real, along with $m_{12}^2, \lambda_5, \lambda_6$ and λ_7, which are complex. If we want to impose the Z_2 symmetry on the potential, we would require $m_{12}^2 = 0$, λ_5 to be real and $\lambda_6 = \lambda_7 = 0$. Then the Z_2-symmetric potential is given by

$$\begin{aligned} V(\Phi_1,\Phi_2) =& -\mu_1^2(\Phi_1^\dagger\Phi_1) - \mu_2^2(\Phi_2^\dagger\Phi_2) + \lambda_1(\Phi_1^\dagger\Phi_1)^2 + \lambda_2(\Phi_2^\dagger\Phi_2)^2 + \lambda_3(\Phi_1^\dagger\Phi_1)(\Phi_2^\dagger\Phi_2) \\ &+ (\lambda_4 - |\lambda_5|)[\mathrm{Re}(\Phi_1^\dagger\Phi_2)]^2 + (\lambda_4 + |\lambda_5|)[\mathrm{Im}(\Phi_1^\dagger\Phi_2)]^2 \end{aligned} \tag{4.6}$$

One can easily check that the potential in equation (4.6) does satisfy the Z_2 symmetry, i.e. the potential is invariant under

$$\Phi_1 \to \Phi_1 \,, \;\; \Phi_2 \to -\Phi_2 \tag{4.7}$$

A complete classification of all possible symmetries (including CP1 and CP2 symmetries) can be found in [30, 33]. It is sometimes useful to consider a reduced parameter space for the 2HDM by using the reduced basis in which $\mathrm{Im}(m_{12}^2) = \mathrm{Im}(\lambda_5) = \mathrm{Im}(\lambda_6) = 0$ and $\lambda_6 = \lambda_7$. In this basis, the requirement of λ_5 being real for the potential to possess the Z_2 symmetry is automatically satisfied.

The equations of motion for the Higgs doublets and the electroweak gauge fields can be derived using the standard action principle. It can be further shown that the equations of motion are satisfied if the energy of the system is minimized [31]. However, it is difficult to obtain analytical solutions for the system of Higgs doublets and gauge fields due to the complexity of the equations. Therefore, we will resort to a numerical method known as the gradient flow technique to obtain solutions for the system. The gradient flow technique will be introduced in chapter 5.

4.1 Parametrizations of the Higgs Doublets

There are different ways to parametrize the Higgs doublets in the 2HDM. The simplest representation is the linear representation:

$$\Phi_1 = \begin{pmatrix} \phi_1 + i\phi_2 \\ \phi_3 + i\phi_4 \end{pmatrix}, \quad \Phi_2 = \begin{pmatrix} \phi_5 + i\phi_6 \\ \phi_7 + i\phi_8 \end{pmatrix} \tag{4.8}$$

The parametrization that will be used in our original results in chapter 6 is realized as an electroweak gauge transformation (EWGT) of the charge-breaking vacua. The charge-breaking vacua are the most general vacua in the 2HDM [28] containing

four vacuum parameters v_1, v_2, v_+ and ξ. They are given by

$$\Phi_1^0 = \frac{1}{\sqrt{2}} \begin{pmatrix} 0 \\ v_1 \end{pmatrix}, \quad \Phi_2^0 = \frac{1}{\sqrt{2}} \begin{pmatrix} v_+ \\ v_2 e^{i\xi} \end{pmatrix} \tag{4.9}$$

The non-zero v_+ implies that the vacua are charge-violating, while the relative phase ξ between the vacua implies that the vacua violate CP. We can parametrize the Higgs doublets using a $\mathrm{SU}(2)_L \times \mathrm{U}(1)_Y$ transformation of the charge-breaking vacua:

$$\Phi_i = U \Phi_i^0 \tag{4.10}$$

where

$$U = e^{i\theta} \exp\left(i \frac{G^a}{v_{\mathrm{SM}}} \frac{\sigma^a}{2} \right) = e^{i\theta} \exp\left(\frac{i \hat{G}^a \sigma^a}{2} \right) , \tag{4.11}$$

θ and $G^a = G^1, G^2, G^3$ are the would-be Goldstone bosons, and v_{SM} is the vacuum expectation value (VEV) of the SM Higgs. In this parametrization, we can see that we have eight parameters in total to represent the vacua, which is the same number of parameters as in the linear representation.

In addition, using the bilinear scalar-field formalism [35, 36, 37], we can introduce a 4-vector R^μ which is invariant under unitary transformations:

$$R^\mu \equiv \Phi^\dagger \sigma^\mu \Phi = \begin{pmatrix} \Phi_1^\dagger \Phi_1 + \Phi_2^\dagger \Phi_2 \\ \Phi_1^\dagger \Phi_2 + \Phi_2^\dagger \Phi_1 \\ -i[\Phi_1^\dagger \Phi_2 - \Phi_2^\dagger \Phi_1] \\ \Phi_1^\dagger \Phi_1 - \Phi_2^\dagger \Phi_2 \end{pmatrix} , \tag{4.12}$$

where $\Phi = (\Phi_1, \Phi_2)^T$. The index μ in σ^μ runs from 0 to 3, with $\sigma^0 = I_2$ and $\sigma^{1,2,3}$ are the Pauli matrices. We can write the general 2HDM potential in terms of the 4-vector R^μ:

$$V = -\frac{1}{2} M_\mu R^\mu + \frac{1}{4} L_{\mu\nu} R^\mu R^\nu , \tag{4.13}$$

where

$$M_\mu = \left(\mu_1^2 + \mu_2^2 , \quad 2\mathrm{Re}(m_{12}^2) , \quad -2\mathrm{Im}(m_{12}^2) , \quad \mu_1^2 - \mu_2^2 \right) , \tag{4.14}$$

$$L_{\mu\nu} = \begin{pmatrix} \lambda_{123} & \mathrm{Re}(\lambda_{67}) & -\mathrm{Im}(\lambda_{67}) & \bar{\lambda}_{12} \\ \mathrm{Re}(\lambda_{67}) & \lambda_4 + \mathrm{Re}(\lambda_5) & -\mathrm{Im}(\lambda_5) & \mathrm{Re}(\bar{\lambda}_{67}) \\ -\mathrm{Im}(\lambda_{67}) & -\mathrm{Im}(\lambda_5) & \lambda_4 - \mathrm{Re}(\lambda_5) & -\mathrm{Im}(\bar{\lambda}_{67}) \\ \bar{\lambda}_{12} & \mathrm{Re}(\bar{\lambda}_{67}) & -\mathrm{Im}(\bar{\lambda}_{67}) & \bar{\lambda}_{123} \end{pmatrix} \tag{4.15}$$

The first term in (4.13) contains the mass terms, while the second term describes the quartic couplings. In (4.15), we have used the notations $\lambda_{ab} = \lambda_a + \lambda_b$, $\bar{\lambda}_{ab} = \lambda_a - \lambda_b$, $\lambda_{abc} = \lambda_a + \lambda_b + \lambda_c$ and $\bar{\lambda}_{abc} = \lambda_a + \lambda_b - \lambda_c$. Since R^μ is invariant under unitary transformations, we can use the charge-breaking vacua to express it in terms of the vacuum parameters:

$$R^\mu = \frac{1}{2} \begin{pmatrix} v_1^2 + v_2^2 + v_+^2 \\ 2v_1 v_2 \cos\xi \\ 2v_1 v_2 \sin\xi \\ v_1^2 - v_2^2 - v_+^2 \end{pmatrix} \tag{4.16}$$

Inverting the relations in (4.16), we can express the vacuum parameters in terms of the components R^μ. In particular, v_+ is related to the components R^μ by

$$v_+^2 = \frac{R_\mu R^\mu}{R^0 + R^3} \tag{4.17}$$

Therefore we can determine whether a solution is charge-violating by looking at either the parameter v_+ or the norm of the 4-vector R^μ. Imposing $R_\mu R^\mu = 0$, which is known as the neutral vacuum condition [35], would imply that $v_+ = 0$, i.e. the solution satisfies the charge symmetry.

To accommodate θ into the formalism, we can utilise the $\mathrm{SU}(2)_L$ invariant $\Phi_1^T i\sigma^2 \Phi_2$ to promote R^μ to a 6-vector R^A [30, 33]:

$$R^A = \begin{pmatrix} \Phi_1^\dagger \Phi_1 + \Phi_2^\dagger \Phi_2 \\ \Phi_1^\dagger \Phi_2 + \Phi_2^\dagger \Phi_1 \\ -i[\Phi_1^\dagger \Phi_2 - \Phi_2^\dagger \Phi_1] \\ \Phi_1^\dagger \Phi_1 - \Phi_2^\dagger \Phi_2 \\ \Phi_1^T i\sigma^2 \Phi_2 - \Phi_2^\dagger i\sigma^2 \Phi_1^* \\ -i[\Phi_1^T i\sigma^2 \Phi_2 + \Phi_2^\dagger i\sigma^2 \Phi_1^*] \end{pmatrix} = \frac{1}{2} \begin{pmatrix} v_1^2 + v_2^2 + v_+^2 \\ 2v_1 v_2 \cos\xi \\ 2v_1 v_2 \sin\xi \\ v_1^2 - v_2^2 - v_+^2 \\ -2v_1 v_+ \cos 2\theta \\ -2v_1 v_+ \sin 2\theta \end{pmatrix} \tag{4.18}$$

To fully span the parameter space of the vacuum manifold, we can choose R^0, R^1, R^2, R^3 and R^4, together with G^1, G^2 and G^3 as our free parameters. There are altogether eight parameters, which agrees with the number of parameters in the vacuum manifold parametrization and the linear representation.

4.2 Mass Matrices

In the 2HDM, we have five physical Higgs states — h, H, A and $H_\pm$. To find the mass matrices, it would be useful to use the following representation of the Higgs doublets:

$$\Phi_1 = \begin{pmatrix} \phi_1^+ \\ \frac{1}{\sqrt{2}}v_1 + \phi_1 + ia_1 \end{pmatrix} , \quad \Phi_2 = e^{i\xi} \begin{pmatrix} \phi_2^+ \\ \frac{1}{\sqrt{2}}v_2 + \phi_2 + ia_2 \end{pmatrix} , \tag{4.19}$$

where ϕ_1^+ and ϕ_2^+ are complex scalar fields. ϕ_1 and ϕ_2 can be expressed as a rotation of the CP-even fields h and H, while a_1 and a_2 can be expressed as a rotation of the CP-odd fields G^0 and A.

$$\begin{pmatrix} \phi_1 \\ \phi_2 \end{pmatrix} = \begin{pmatrix} c_\alpha & -s_\alpha \\ s_\alpha & c_\alpha \end{pmatrix} \begin{pmatrix} h \\ H \end{pmatrix} , \quad \begin{pmatrix} a_1 \\ a_2 \end{pmatrix} = \begin{pmatrix} c_\beta & -s_\beta \\ s_\beta & c_\beta \end{pmatrix} \begin{pmatrix} G^0 \\ A \end{pmatrix} , \tag{4.20}$$

where $s_\alpha = \sin\alpha$ and $c_\alpha = \cos\alpha$, and similar short-hand notations are used in s_β and c_β. G^0 is one of the would-be Goldstone bosons. Since the Z_2-symmetric 2HDM is CP-preserving, the CP-odd states do not mix with the CP-even states and we have $\xi = 0$ [31]. Substituting the representations of the Higgs doublets in (4.19) back into the Z_2-symmetric potential in (4.6), we can then calculate the following mass matrices:

$$\mathcal{M}^2_{h,H} = \frac{1}{2}\left(\frac{\partial^2 V}{\partial\phi_i \partial\phi_j}\right) = \begin{pmatrix} 2\lambda_1 v_1^2 & \tilde{\lambda}_{345} v_1 v_2 \\ \tilde{\lambda}_{345} v_1 v_2 & 2\lambda_2 v_2^2 \end{pmatrix} \tag{4.21}$$

$$\mathcal{M}^2_{A} = \frac{1}{2}\left(\frac{\partial^2 V}{\partial a_i \partial a_j}\right) = |\lambda_5| \begin{pmatrix} v_2^2 & -v_1 v_2 \\ -v_1 v_2 & v_1^2 \end{pmatrix} \tag{4.22}$$

$$\mathcal{M}^2_{H^\pm} = \left(\frac{\partial^2 V}{\partial\phi_i^+\partial\phi_j^-}\right) = -\frac{1}{2}(\lambda_4 - |\lambda_5|)\begin{pmatrix} v_2^2 & -v_1v_2 \\ -v_1v_2 & v_1^2 \end{pmatrix} \tag{4.23}$$

The masses of the physical scalars can be calculated as the non-zero eigenvalues of the mass matrices to be

$$M_h^2 = \lambda_1 v_1^2 + \lambda_2 v_2^2 - \sqrt{(\lambda_1 v_1^2 - \lambda_2 v_2^2)^2 + \tilde{\lambda}_{345}^2 v_1^2 v_2^2}\,, \tag{4.24}$$

$$M_H^2 = \lambda_1 v_1^2 + \lambda_2 v_2^2 + \sqrt{(\lambda_1 v_1^2 - \lambda_2 v_2^2)^2 + \tilde{\lambda}_{345}^2 v_1^2 v_2^2}\,, \tag{4.25}$$

$$M_A^2 = |\lambda_5| v_{\rm SM}^2\,, \tag{4.26}$$

$$M_{H^\pm}^2 = -\frac{1}{2}(\lambda_4 - |\lambda_5|) v_{\rm SM}^2\,, \tag{4.27}$$

where $\tilde{\lambda}_{345} = \lambda_3 + \lambda_4 - |\lambda_5|$ and $v_{\rm SM} = 246\,\text{GeV}$ is the VEV of the SM Higgs. The VEVs of the Higgs doublets are related to $v_{\rm SM}$ by the mixing angle β for the CP-odd scalars:

$$v_1^0 = c_\beta v_{\rm SM}\,, \quad v_2^0 = s_\beta v_{\rm SM} \tag{4.28}$$

Chapter 5

Gradient Flow

In a field theory with N scalar fields, the Lagrangian $L[\phi_k, \partial_\mu \phi_k]$ is a functional of $\phi_k(x)$ and $\partial_\mu \phi_k(x)$, where $\mu = 0$ corresponds to time while $\mu = 1, 2, 3$ correspond to the spatial dimensions, and $k = 1, 2, ..., N$ denotes the different scalar fields. Often we want to find time-independent solutions $\phi_k(\mathbf{x})$ which minimize the energy of the system. In most cases the solutions cannot be obtained analytically, so we need to resort to numerical methods. Given a time-independent energy density, we can use a numerical technique called the gradient flow technique to find the minimum energy field configurations.

In this section, the gradient flow technique will be explained. The technique will first be applied to the ϕ^4 theory as an example, where the analytical field solution is known. Then gradient flow will be applied to the Z_2-symmetric Two Higgs Doublet Model (2HDM) to look for minimum energy solutions using two different parametrizations.

5.1 Theory

Consider a complex scalar field theory with N complex scalar fields $\phi_i, i = 1, 2, ...N$. The Lagrangian density for the theory is given by

$$\mathcal{L} = \sum_{i=1}^{N} (\dot{\phi_i^*}\dot{\phi_i} - \nabla{\phi_i}^* \cdot \nabla\phi_i) - V(\phi_1, \phi_2, ..., \phi_N) \,, \tag{5.1}$$

where the fields $\phi_i = \phi_i(x)$ can contain time dependence in general. The Hamiltonian density of the theory is given by

$$\mathcal{H} = \sum_{i=1}^{N} (\pi_i\dot{\phi_i} + \pi_i^*\dot{\phi_i^*}) - \mathcal{L} = \sum_{i=1}^{N} (\dot{\phi_i^*}\dot{\phi_i} + \nabla{\phi_i}^* \cdot \nabla\phi_i) + V(\phi_1, \phi_2, ..., \phi_N) \,, \tag{5.2}$$

where $\pi_i = \frac{\partial\mathcal{L}}{\partial\dot{\phi_i}} = \dot{\phi_i^*}$ is the conjugate momentum to ϕ_i. If the fields are time-independent, we will have $\pi_i = 0$ so $\mathcal{H} = -\mathcal{L}$. We can then write the total energy of the system as a functional

$$E = \int_{-\infty}^{\infty} d^3\mathbf{x}\, \mathcal{H} = -\int_{-\infty}^{\infty} d^3\mathbf{x}\, \mathcal{L} = \int_{-\infty}^{\infty} d^3\mathbf{x} \left(\sum_{i=1}^{N} (\nabla{\phi_i}^* \nabla\phi_i) + V(\phi_1, \phi_2, ..., \phi_N) \right) \tag{5.3}$$

The solutions for $\phi_i(\mathbf{x})$ are those that minimize the energy of the system. Often we want to solve the field equations under specific boundary conditions of the fields. In many cases it is difficult to find solutions analytically, so we will need to use numerical methods.

In the gradient flow technique, we introduce a fictitious time parameter t so that our fields become

$$\phi_i = \phi_i(\mathbf{x}, t) \tag{5.4}$$

We want our field solutions to minimize the total energy of the system, so we set

$$\dot{\phi_i} = -\frac{\delta E}{\delta\phi_i^*} \tag{5.5}$$

There is a negative sign before the functional derivative because we want the

fields to evolve in a way such that the energy decreases and eventually reaches a minimum. From equation (5.3), we can show that under the infinitesimal variation $\phi_i^* \to \phi_i^* + \delta\phi_i^*$:

$$\delta E = \int d^3\mathbf{x} \left(\nabla \delta\phi_i^* \nabla\phi_i + \frac{\partial V}{\partial \phi_i^*} \delta\phi_i^* \right) = \int d^3\mathbf{x} \left(-\nabla^2\phi_i + \frac{\partial V}{\partial \phi_i^*} \right) \delta\phi_i^* \,, \tag{5.6}$$

where integration by part was used in the last step. Putting this back into equation (5.5) we will obtain the following gradient flow equation:

$$\dot{\phi}_i = -\frac{\delta E}{\delta \phi_i^*} = \nabla^2\phi_i - \frac{\partial V}{\partial \phi_i^*} \tag{5.7}$$

Note that the RHS of equation (5.7) looks similar to terms in the Euler-Lagrange equation for the field ϕ_i. This is because for a time-independent theory $E = -L$, as we have seen before. When we evolve the field ϕ_i with the fictitious time t, the LHS of equation (5.7) will tend to zero as $t \to \infty$. Therefore as ϕ_i becomes static, equation (5.7) will become the Euler-Lagrange equation, which gives us the solution for ϕ_i.

In the following we will consider a 1-dimensional problem with $\phi = \phi(x)$. To solve the system numerically we need to truncate the x interval from $(-\infty, \infty)$ to $[-R, R]$ for some value R. Then we discretize our fields ϕ_i in terms of the spatial and fictitious time components. We label the time component with an upper index a and the spatial component with a lower index b. We can then write the time and spatial derivatives of the field as

$$\dot{\phi}_i = \frac{\phi_{i,b}^{a+1} - \phi_{i,b}^a}{\Delta t} \tag{5.8}$$

$$\frac{\partial^2\phi_i}{\partial x^2} = \frac{\phi_{i,b+1}^a + \phi_{i,b-1}^a - 2\phi_{i,b}^a}{(\Delta x)^2} \,, \tag{5.9}$$

where Δt and Δx are our time step and spatial step respectively.

If we have an initial guess of $\phi_{i,b}^0, b = 1, ..., N_x$, where N_x is the total number of spatial steps, we can use equation (5.7) to find $\phi_{i,b}^1$. Iterating the process for a

sufficiently large number of time steps would give us numerical approximations for the field configurations $\phi_i(x)$ which minimize the total energy of the system.

5.2 Gradient Flow in the ϕ^4 Theory

We will apply the gradient flow technique to the 1-dimensional Goldstone model with the ϕ^4 potential, which we have discussed in section 2.3. As a reminder, the Lagrangian of the theory is given by

$$\mathcal{L} = -\frac{1}{2}\left(\frac{d\phi}{dx}\right)^2 - \frac{\lambda}{4}\left(\phi^2 - \eta^2\right)^2 \tag{5.10}$$

The equation of motion for ϕ is given by $\frac{d^2\phi}{dx^2} - \lambda\phi(\phi^2 - \eta^2) = 0$. We have seen that one analytical solution for this equation is $\phi(x) = \eta \tanh\left(\sqrt{\frac{\lambda}{2}}\eta x\right)$, which is shown in Figure 2.1(b).

Now we will try to use the gradient flow technique to find the solution for $\phi(x)$ to see if it matches the analytical solution. We truncate the interval $x \in (-\infty, \infty)$ into $x \in [-R, R]$. We have seen that the analytical solution interpolates between the two vacua $\pm\eta$ such that $\lim_{x\to\pm\infty} \phi(x) = \pm\eta$. We therefore choose the boundary conditions $\phi(x = \pm R) = \pm\eta$ for our gradient flow simulation.

Since in this theory $\phi^* = \phi$, using equation (5.7) the gradient flow equation can be expressed as

$$\dot{\phi} = \frac{d^2\phi}{dx^2} - \frac{dV}{d\phi} \tag{5.11}$$

Our potential is $V = \frac{\lambda}{4}(\phi^2 - \eta^2)^2$. Using equations (5.8) and (5.9) to discretize the time and spatial derivatives of ϕ, we obtain the following gradient flow equation:

$$\phi_b^{a+1} = \phi_b^a + r(\phi_{b+1}^a + \phi_{b-1}^a - 2\phi_b^a) - \Delta t\lambda\phi_b^a[(\phi_b^a)^2 - \eta^2]\,, \tag{5.12}$$

where $r = \frac{\Delta t}{(\Delta x)^2}$. As before, the upper index a denotes the time component of ϕ and the lower index b denotes the spatial component. The total number of spatial

points for interpolation is given by $N_x = \frac{2R}{\Delta x}$. We make the initial guess for $\phi(x)$ to be a straight line between the points $(-R, -\eta)$ and (R, η), which can be written as

$$\phi_b^0 = \eta \left(\frac{b\Delta x}{R} - 1 \right) , \tag{5.13}$$

where $b = 0, 1, 2, ..., N_x$. We use the parameters $\lambda = 1, \eta = 1\,\text{GeV}, R = 20, N_x = 5000$ and $r = 0.05$. An example code can be found in [29]. A total of 2.2×10^6 time steps have been used in the gradient flow. The evolution of the field during the gradient flow is shown in Figure 5.1(a), while the evolution of the energy is shown in Figure 5.1(b).

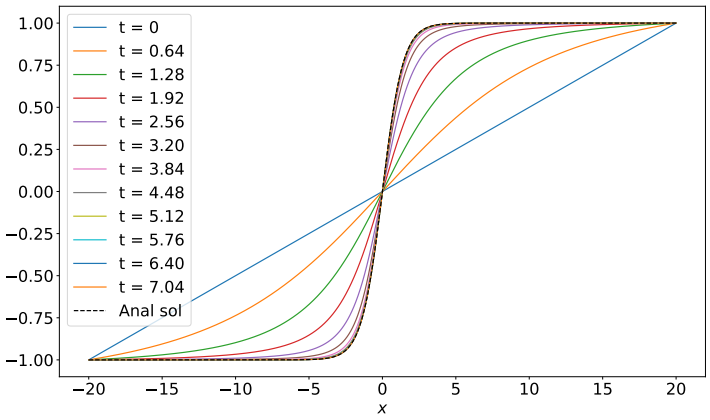

(a) Evolution of $\phi(x)$ with fictitious time t during the gradient flow for the ϕ^4 theory. A straight line connecting the two vacua $\pm\eta$ at the boundaries is used as the initial guess for $\phi(x)$. The final field profile closely matches the analytical solution $\phi(x) = \eta \tanh\left(\sqrt{\frac{\lambda}{2}}\eta x\right)$.

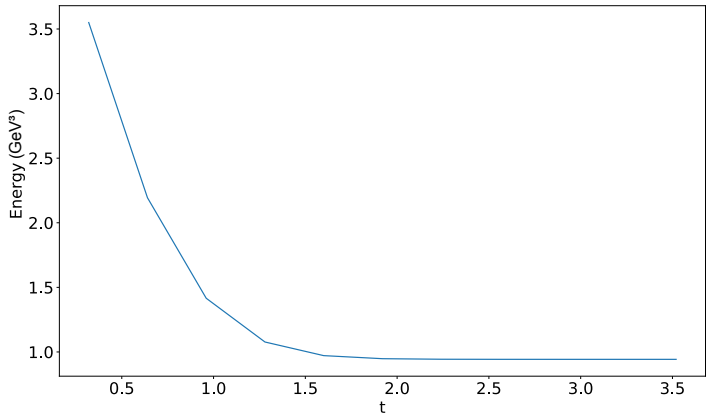

(b) Evolution of the energy during the gradient flow. The energy gradually decreases until approaching the minimum energy of 0.942808 GeV^3, which is within 10^{-6} of the analytical value $\frac{2\sqrt{2}}{3}$ GeV^3.

Figure 5.1: Using the gradient flow technique to find the ground state field configuration $\phi(x)$ in the ϕ^4 theory. The parameters $\lambda = 1$ and $\eta = 1\,\text{GeV}$ are used.

5.3 Gradient flow in the Z_2-symmetric 2HDM

While we can solve for the ground state solution of the 1-dimensional Goldstone model analytically, it is often not easy to find analytical solutions for other models. In this thesis, we are interested in studying domain walls in the Z_2-symmetric 2HDM by solving the equations of motion for the Higgs doublets. These equations are coupled second-order differential equations, which are hard to solve analytically. Therefore, we will apply the gradient flow technique to obtain the ground state solutions of the model [30, 31]. In one dimension, the energy density of the Z_2-symmetric 2HDM, which is the T^{00} component of the energy-stress tensor, is given by

$$\mathcal{E}(\Phi_1, \Phi_2) = \frac{d\Phi_1^\dagger}{dx}\frac{d\Phi_1}{dx} + \frac{d\Phi_2^\dagger}{dx}\frac{d\Phi_2}{dx} + V(\Phi_1, \Phi_2) + V_0 \,, \tag{5.14}$$

where $V(\Phi_1, \Phi_2)$ is the Z_2-symmetric potential given in (4.6). V_0 is a constant introduced so that the minimum energy density is zero. As before, we would like to use the gradient flow technique to find solutions which minimize the energy of the system $E = \int dx\, \mathcal{E}(\Phi_1, \Phi_2)$. In three spatial dimensions, this represents the energy per unit area of the system.

CP-preserving Vacua

To begin with, we choose the CP-preserving vacua as the ansatz for the Higgs doublets:

$$\Phi_1^0(x) = \frac{1}{\sqrt{2}}\begin{pmatrix} 0 \\ v_1(x) \end{pmatrix}, \quad \Phi_2^0(x) = \frac{1}{\sqrt{2}}\begin{pmatrix} 0 \\ v_2(x) \end{pmatrix} \tag{5.15}$$

Note that the CP-preserving vacua can be obtained by setting $v_+ = 0$ and $\xi = 0$ in the charge-breaking vacua in (4.9). Even though this case is more restrictive, it is the simplest ansatz since there are only two vacuum parameters involved. Substituting the ansatz into (5.14), the energy density is given by

$$\mathcal{E} = \frac{1}{2}\left(\frac{dv_1}{dx}\right)^2 + \frac{1}{2}\left(\frac{dv_2}{dx}\right)^2 - \frac{1}{2}\mu_1^2 v_1^2 - \frac{1}{2}\mu_2 v_2^2 + \frac{1}{4}\lambda_1 v_1^4 + \frac{1}{4}\lambda_2 v_2^4 + \frac{1}{4}(\lambda_{34} - |\lambda_5|)v_1^2 v_2^2 + V_0 \tag{5.16}$$

To simplify the equations, we can introduce the following dimensionless quantities [30]

$$\hat{x} = \mu_2 x \,, \;\; \hat{v}_{1,2} = \frac{v_{1,2}(x)}{\eta} \,, \;\; \hat{E} = \frac{\lambda_2 E}{\mu_2^3} \,, \tag{5.17}$$

and new parameters

$$\mu^2 = \frac{\mu_1^2}{\mu_2^2} \,, \;\; \lambda = \frac{\lambda_1}{\lambda_2} \,, \;\; g = \frac{\lambda_{34} - |\lambda_5|}{2\lambda_2} \,, \;\; \eta = \frac{\mu_2}{\sqrt{\lambda_2}} \tag{5.18}$$

The dimensionless energy density is then given by

$$\hat{\mathcal{E}} = \frac{1}{2}\left(\frac{d\hat{v}_1}{d\hat{x}}\right)^2 + \frac{1}{2}\left(\frac{d\hat{v}_2}{d\hat{x}}\right)^2 - \frac{1}{2}\mu^2\hat{v}_1^2 - \frac{1}{2}\hat{v}_2^2 + \frac{1}{4}\lambda\hat{v}_1^4 + \frac{1}{4}\hat{v}_2^4 + \frac{g}{2}\hat{v}_1^2\hat{v}_2^2 + \hat{V}_0 \tag{5.19}$$

The equations of motion for the rescaled fields are

$$\begin{aligned} \frac{d^2\hat{v}_1}{d\hat{x}^2} &= \hat{v}_1[-\mu^2 + \lambda(\hat{v}_1)^2 + g(\hat{v}_2)^2] \\ \frac{d^2\hat{v}_2}{d\hat{x}^2} &= \hat{v}_2[-1 + (\hat{v}_2)^2 + g(\hat{v}_1)^2] \end{aligned} \tag{5.20}$$

We choose the range $x \in [-R, R]$, where $R = 20$. We impose the boundary conditions $\hat{v}_1(\pm R) = \hat{v}_1^0$ and $\hat{v}_2(\pm R) = \pm\hat{v}_2^0$, where $\hat{v}_1^0$ and $\hat{v}_2^0$ are the vacuum expectation values (VEVs) of $\hat{v}_1$ and $\hat{v}_2$ respectively. The VEVs can be calculated by imposing the extremization condition and the neutral vacuum condition on the potential in the bilinear scalar-field formalism [30]. Using our new parameters, the VEVs can be expressed as

$$\hat{v}_1^0 = \sqrt{\frac{\mu^2 - g}{\lambda - g^2}} \,, \quad \hat{v}_2^0 = \sqrt{\frac{\lambda - \mu^2 g}{\lambda - g^2}} \tag{5.21}$$

The parameters μ^2, λ and g should be chosen such that the potential is bounded from below and has a global minimum [30]. For our gradient flow simulation, we use the parameter set $\{\mu^2, \lambda, g\} = \{1, 1, 0.5\}$. We also choose the number of spatial points to be $N_x = 5000$, and $r = \frac{\Delta t}{\Delta x^2} = 0.05$. The initial guess for $\hat{v}_1$ is a horizontal line between $(-R, \hat{v}_1^0)$ and $(R, \hat{v}_1^0)$, while the initial guess for $\hat{v}_2$ is a straight line from $(-R, -\hat{v}_2^0)$ to $(R, \hat{v}_2^0)$. $\hat{V}_0$ is chosen to be 0.332 so that $\hat{\mathcal{E}}(\pm R) = 0$. A total of

3.4×10^6 time steps have been used in the gradient flow, with the results shown in Figure 5.2.

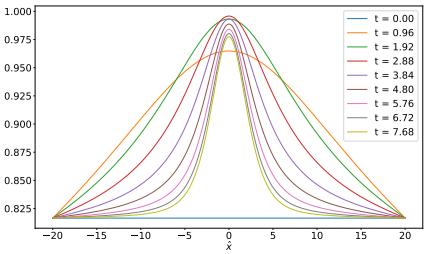

(a) Evolution of $\hat{v}_1(\hat{x})$ during the gradient flow.

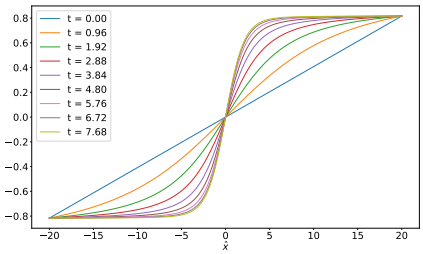

(b) Evolution of $\hat{v}_2(\hat{x})$ during the gradient flow.

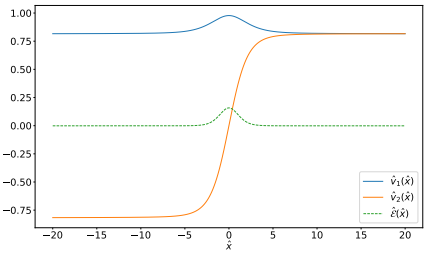

(c) The ground state field profiles and the energy density.

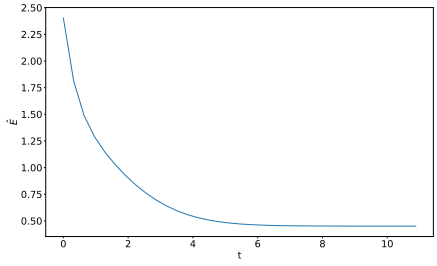

(d) Evolution of $\hat{E}$ during the gradient flow.

Figure 5.2: Using the gradient flow technique to find the ground state field configuration in the Z_2-symmetric 2HDM with CP-preserving vacua. The parameters used are $\mu^2 = \frac{\mu_1^2}{\mu_2^2} = 1$, $\lambda = \frac{\lambda_1}{\lambda_2} = 1$ and $g = \frac{\lambda_{34} - |\lambda_5|}{2\lambda_2} = 0.5$. There is a domain wall feature in $\hat{v}_2$ near the origin. The energy density peaks at the domain wall. The final energy of the system is found to be $\hat{E} = 0.450$.

Charge-breaking Vacua

To extend our study of vacua in the Z_2-symmetric 2HDM, we choose the charge-breaking vacua as our next ansatz:

$$\Phi_1^0(x) = \frac{1}{\sqrt{2}} \begin{pmatrix} 0 \\ v_1(x) \end{pmatrix} , \quad \Phi_2^0(x) = \frac{1}{\sqrt{2}} \begin{pmatrix} v_+(x) \\ v_2(x) e^{i\xi(x)} \end{pmatrix} , \tag{5.22}$$

We can then write the Z_2-symmetric potential in equation (4.6) in terms of the vacuum manifold parameters:

$$\begin{aligned} V = &-\frac{1}{2}\mu_1^2 v_1^2 - \frac{1}{2}\mu_2^2(v_2^2 + v_+^2) + \frac{1}{4}\lambda_1 v_1^4 + \frac{1}{4}\lambda_2\left(v_2^2 + v_+^2\right)^2 \\ &+ \frac{1}{4}\lambda_3 v_1^2 v_+^2 + \frac{1}{4}(\lambda_{34} - |\lambda_5|c_{2\xi})v_1^2 v_2^2 \,, \end{aligned} \tag{5.23}$$

The energy density of the Z_2-symmetric 2HDM is given by

$$\mathcal{E} = \frac{1}{2}\left(\frac{dv_1}{dx}\right)^2 + \frac{1}{2}\left(\frac{dv_2}{dx}\right)^2 + \frac{1}{2}v_2^2\left(\frac{d\xi}{dx}\right)^2 + \frac{1}{2}\left(\frac{dv_+}{dx}\right)^2 + V + V_0 \tag{5.24}$$

The gradient flow equations for the vacuum manifold parameters are then given by

$$\begin{aligned} \frac{\partial v_1}{\partial t} &= \frac{\partial^2 v_1}{\partial x^2} + \mu_1^2 v_1 - \lambda_1 v_1^3 - \frac{1}{2}\lambda_3 v_1 v_+^2 - \frac{1}{2}(\lambda_{34} - |\lambda_5|c_{2\xi})v_1 v_2^2 \\ \frac{\partial v_2}{\partial t} &= \frac{\partial^2 v_2}{\partial x^2} - v_2\left(\frac{\partial \xi}{\partial x}\right)^2 + \mu_2^2 v_2 - \lambda_2 v_2(v_2^2 + v_+^2) - \frac{1}{2}(\lambda_{34} - |\lambda_5|c_{2\xi})v_1^2 v_2 \\ \frac{\partial \xi}{\partial t} &= v_2^2\frac{\partial^2 \xi}{\partial x^2} + 2v_2\left(\frac{\partial v_2}{\partial x}\right)\left(\frac{\partial \xi}{\partial x}\right) - \frac{1}{2}|\lambda_5| v_1^2 v_2^2 s_{2\xi} \\ \frac{\partial v_+}{\partial t} &= \frac{\partial^2 v_+}{\partial x^2} + \mu_2^2 v_+ - \lambda_2 v_+(v_2^2 + v_+^2) - \frac{1}{2}\lambda_3 v_1^2 v_+ \end{aligned} \tag{5.25}$$

We rescale the length and energy so that they become dimensionless:

$$\begin{aligned} &\hat{x} = M_h x \,, \quad \hat{v}_i = \frac{v_i}{v_{\rm SM}} \,,\ i = 1, 2, + \,, \\ &\hat{\mathcal{E}} = \frac{\mathcal{E}}{M_h^2 v_{\rm SM}^2} \,, \end{aligned} \tag{5.26}$$

where $M_h = 125\,\text{GeV}$ is the SM Higgs mass and $v_{\rm SM} = 246\,\text{GeV}$ is the VEV of the SM Higgs. These physical quantities are determined by experiment [38]. We also rescale the following parameters to facilitate the rescaling of the energy density:

$$\hat{\mu}_1^2 = \frac{\mu_1^2}{M_h^2} \,, \quad \hat{\mu}_2^2 = \frac{\mu_2^2}{M_h^2} \,, \quad \hat{\lambda}_i = \frac{\lambda_i v_{\rm SM}^2}{M_h^2} \,,\ i = 1, 2, 3, 4, 5 \tag{5.27}$$

So now we can rewrite the gradient flow equations in (5.25) in terms of the rescaled quantities — simply replace all variables and parameters with the rescaled ones.

In the 2HDM, we have five physical Higgs states — h, H, A and $H_\pm$. In the gradient flow simulation we choose $M_H = M_A = M_{H_\pm} = 200\,\text{GeV}$. For the angles α and β, which are the mixing angles for the CP-even/odd scalars respectively, we choose values such that $\tan\beta = 0.85, \cos(\alpha-\beta) = 1.0$. To relate the parameters in the potential to these physical quantities, we can consider the diagonalization of the mass matrix $\mathcal{M}^2_{h,H}$ in (4.21) using the mixing angle α [34]:

$$\mathcal{M}^2_{h,H} = \begin{pmatrix} 2\lambda_1 v_1^2 & \tilde{\lambda}_{345} v_1 v_2 \\ \tilde{\lambda}_{345} v_1 v_2 & 2\lambda_2 v_2^2 \end{pmatrix} = \begin{pmatrix} c_\alpha & -s_\alpha \\ s_\alpha & c_\alpha \end{pmatrix} \begin{pmatrix} M_h^2 & 0 \\ 0 & M_H^2 \end{pmatrix} \begin{pmatrix} c_\alpha & s_\alpha \\ -s_\alpha & c_\alpha \end{pmatrix} \tag{5.28}$$

We can then find the following relations:

$$\lambda_1 = \frac{M_h^2 c_\alpha^2 + M_H^2 s_\alpha^2}{2 c_\beta^2 v_{\text{SM}}^2} \tag{5.29}$$

$$\lambda_2 = \frac{M_h^2 s_\alpha^2 + M_H^2 c_\alpha^2}{2 s_\beta^2 v_{\text{SM}}^2} \tag{5.30}$$

$$\tilde{\lambda}_{345} = \frac{(M_h^2 - M_H^2) c_\alpha s_\alpha}{c_\beta s_\beta v_{\text{SM}}^2} \tag{5.31}$$

We can also write μ_1^2 and μ_2^2 in terms of the physical parameters. We first note that the VEVs of the Z_2-symmetric 2HDM can be calculated and expressed in terms of the potential parameters [30]:

$$(v_1^0)^2 = \frac{4\lambda_2\mu_1^2 - 2\tilde{\lambda}_{345}\mu_2^2}{4\lambda_1\lambda_2 - \tilde{\lambda}_{345}^2}\,, \quad (v_2^0)^2 = \frac{4\lambda_1\mu_2^2 - 2\tilde{\lambda}_{345}\mu_1^2}{4\lambda_1\lambda_2 - \tilde{\lambda}_{345}^2} \tag{5.32}$$

Inverting the relations in (5.32), and using (4.28), we can obtain the following:

$$\begin{aligned} \mu_1^2 &= \frac{1}{2} v_{\text{SM}}^2 \left(2\lambda_1 c_\beta^2 + \tilde{\lambda}_{345} s_\beta^2\right) \\ \mu_2^2 &= \frac{1}{2} v_{\text{SM}}^2 \left(2\lambda_2 s_\beta^2 + \tilde{\lambda}_{345} c_\beta^2\right) \end{aligned} \tag{5.33}$$

Substituting (5.29)-(5.31) into (5.33), we can write μ_1^2 and μ_2^2 in terms of the physical quantities:

$$\begin{aligned}\mu_1^2 &= \frac{1}{2}[M_h^2 c_\alpha^2 + M_H^2 s_\alpha^2 + (M_h^2 - M_H^2) c_\alpha s_\alpha \tan\beta] \\ \mu_2^2 &= \frac{1}{2}[M_h^2 s_\alpha^2 + M_H^2 c_\alpha^2 + (M_h^2 - M_H^2) c_\alpha s_\alpha \cot\beta]\end{aligned} \tag{5.34}$$

Finally, we can relate the parameters $\lambda_4, |\lambda_5|$ to the mass of the CP-odd scalar A in (4.26) and the masses of the charged scalars $H^\pm$ in (4.27):

$$\begin{aligned}(\lambda_4 - |\lambda_5|) &= -\frac{2M_{H^\pm}^2}{v_{\rm SM}^2} \\ (\lambda_4 + |\lambda_5|) &= \frac{2(M_A^2 - M_{H^\pm}^2)}{v_{\rm SM}^2}\end{aligned} \tag{5.35}$$

Using (5.31) and (5.35), we obtain the following expression for λ_3:

$$\lambda_3 = \frac{(M_h^2 - M_H^2)\, c_\alpha s_\alpha + 2M_{H^\pm}^2 c_\beta s_\beta}{c_\beta s_\beta v_{\rm SM}^2} \tag{5.36}$$

For the gradient flow simulation, we choose the range $x \in [-R, R]$, where $R = 20$. We impose the boundary conditions: $\hat{v}_1(\pm R) = \hat{v}_1^0$, $\hat{v}_2(\pm R) = \pm\hat{v}_2^0$, $\xi(\pm R) = 0$, $\hat{v}_+(\pm R) = 0$, where $\hat{v}_1^0$ and $\hat{v}_2^0$ are the VEVs in (5.32) which are rescaled following the procedures in (5.27) .

The initial guesses are a horizontal line for $\hat{v}_1$, a straight line for $\hat{v}_2$ and quadratic curves for ξ and $\hat{v}_+$ with y-intercepts of 0.5. The number of spatial interpolation points is $N_x = 5000$. We also choose $r = \frac{\Delta t}{(\Delta x)^2} = 0.05$. The number of spatial interpolation points affects the size of the spatial grid used in the simulation, and hence the precision of the result. The number of spatial points is chosen to maintain a balance between computational time and precision. On the other hand, the size of the time step is chosen to ensure proper convergence of the results.

A total of 3.0×10^6 time steps have been used. For the CP-preserving vacua, the convergence of the energy was used to determine whether the ground state

solution has been reached. However, it is found that for the charge-breaking vacua the parameter ξ takes longer to converge than the energy. Therefore, the gradient flow simulation has been run until all the parameters reach the steady state.

The results of the gradient flow of the vacuum parameters are shown in Figure 5.3(a), while the corresponding R-space profiles are plotted in Figure 5.3(b).

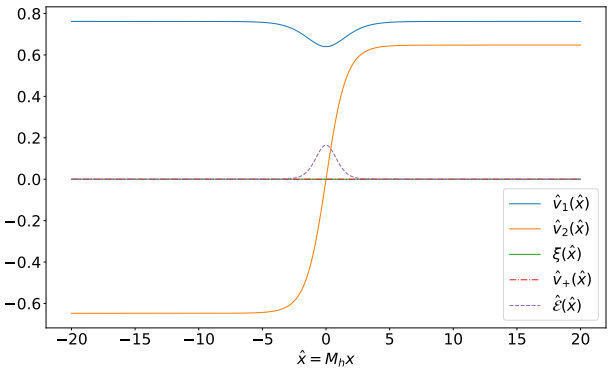

(a) Gradient flow results for the vacuum manifold parameters, showing a kink solution in v_2.

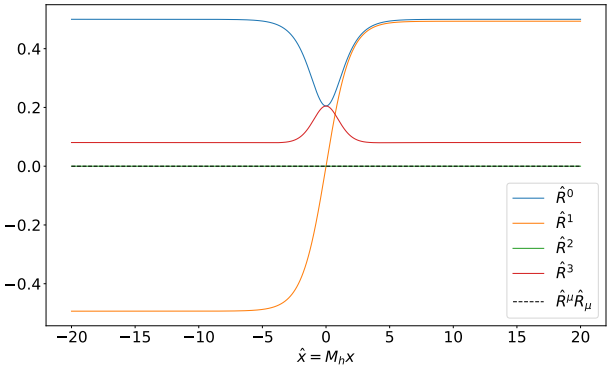

(b) The corresponding R-space profiles using the results in (a). There is a clear kink solution in R^1.

Figure 5.3: Using gradient flow to find the minimum energy field configuration in the Z_2-symmetric 2HDM with the charge-violating vacua. The parameters are chosen to be $M_H = M_A = M_{H^\pm} = 200\,\text{GeV}$, $\tan\beta = 0.85$ and $\cos(\alpha - \beta) = 1.0$. The final energy of the solution is found to be 0.354.

$\hat{V}_0$ in $\hat{\mathcal{E}}$ has been chosen to be 0.125 so that $\hat{\mathcal{E}}(\pm R) = 0$. We can see that $R^\mu R_\mu = 0$ and $v_+ = 0$ for all x, which means that the solutions satisfy the neutral vacuum condition, i.e. charge symmetry is satisfied.

From Figure 5.3, the width of the domain wall can be found to be approximately $\frac{10}{M_h}$, which is $0.08\,\mathrm{GeV}^{-1}$. This shows that the field interpolates between the two VEVs over a small distance. The energy per unit area of the domain wall solution is calculated to be $2.68 \times 10^6\,\mathrm{GeV}^3$. Considering the energy within an area of $1\,\mathrm{GeV}^{-2}$ (or $3.88 \times 10^{-32}\,\mathrm{m}^2$), it is a lot bigger than the electroweak scale. Once the domain walls are formed, their energy density scales as t^{-1}, as shown in equation (2.19).

Chapter 6

Charge-violating Kink Solutions in the Z_2-Symmetric 2HDM

The charge-breaking vacua are given by

$$\Phi_1^0 = \frac{1}{\sqrt{2}} \begin{pmatrix} 0 \\ v_1 \end{pmatrix} \ , \ \Phi_2^0 = \frac{1}{\sqrt{2}} \begin{pmatrix} v_+ \\ v_2 e^{i\xi} \end{pmatrix} \tag{6.1}$$

We can consider a general parametrization of the Higgs doublet by performing the electroweak gauge transformation U on the charge-breaking vacua in (6.1):

$$\Phi_i = U\Phi_i^0 \ , \tag{6.2}$$

where we write U as

$$U = \exp\left(i\frac{G^a(x)}{v_{\rm SM}}\frac{\sigma^a}{2}\right)e^{i\theta(x)} = \exp\left(\frac{i\hat{G}^a(x)\sigma^a}{2}\right)e^{i\theta(x)} \ , \tag{6.3}$$

and $v_{\rm SM}$ is the vacuum expectation value (VEV) of the Standard Model (SM) Higgs.

Recall that the energy density of the 2HDM is given by

$$\mathcal{E} = \frac{d\Phi_1^\dagger}{dx}\frac{d\Phi_1}{dx} + \frac{d\Phi_2^\dagger}{dx}\frac{d\Phi_2}{dx} + V(\Phi_1, \Phi_2) \tag{6.4}$$

In the Z_2-symmetric 2HDM, the potential is given by

$$\begin{aligned} V(\Phi_1, \Phi_2) = &- \mu_1^2(\Phi_1^\dagger\Phi_1) - \mu_2^2(\Phi_2^\dagger\Phi_2) + \lambda_1(\Phi_1^\dagger\Phi_1)^2 + \lambda_2(\Phi_2^\dagger\Phi_2)^2 + \lambda_3(\Phi_1^\dagger\Phi_1)(\Phi_2^\dagger\Phi_2) \\ &+ (\lambda_4 - |\lambda_5|)[\mathrm{Re}(\Phi_1^\dagger\Phi_2)]^2 + (\lambda_4 + |\lambda_5|)[\mathrm{Im}(\Phi_1^\dagger\Phi_2)]^2 \end{aligned} \tag{6.5}$$

Note that if we write the doublets in the form of equation (6.2), the unitary matrix U will drop out of the potential $V(\Phi_1, \Phi_2)$ since $U^\dagger U = I$. In this thesis, we will focus on the cases where only one of the $\hat{G}^a$ is non-zero in the electroweak gauge transformation given in (6.3). This corresponds to choosing a particular axis of the SU(2) rotation. Making this simplification, we have

$$\frac{dU}{dx} = i\left(\frac{d\theta}{dx} + \frac{d\hat{G}^a}{dx}\frac{\sigma^a}{2}\right)U\,, \tag{6.6}$$

where the index a is not summed over. Substituting (6.2) into (6.4), and using (6.6), we find that the kinetic part of the energy density can be expressed as

$$\begin{aligned} \mathcal{E}_{\mathrm{kin}} = &\left|\frac{d\Phi_i^0}{dx}\right|^2 + |\Phi_i^0|^2\left[\left(\frac{d\theta}{dx}\right)^2 + \frac{1}{4}\left(\frac{d\hat{G}^a}{dx}\right)^2\right] + \Phi_i^{0\dagger}U^\dagger\left(\frac{d\theta}{dx}\right)\left(\frac{d\hat{G}^a}{dx}\right)\sigma^a U\Phi_i^0 \\ &+ \left[i\frac{d\Phi_i^{0\dagger}}{dx}U^\dagger\left(\frac{d\theta}{dx} + \frac{d\hat{G}^a}{dx}\frac{\sigma^a}{2}\right)U\Phi_i^0 + \mathrm{h.c.}\right] \end{aligned} \tag{6.7}$$

Since U involves the exponentiation of only one Pauli matrix σ^a, it commutes with

the Pauli matrix itself. The energy density can then be further simplified to be

$$\begin{aligned}\mathcal{E}_{\text{kin}} =& \left|\frac{d\Phi_i^0}{dx}\right|^2 + |\Phi_i^0|^2 \left[\left(\frac{d\theta}{dx}\right)^2 + \frac{1}{4}\left(\frac{d\hat{G}^a}{dx}\right)^2\right] + \Phi_i^{0\dagger}\left(\frac{d\theta}{dx}\right)\left(\frac{d\hat{G}^a}{dx}\right)\sigma^a\Phi_i^0 \\ &+ \left[i\frac{d\Phi_i^{0\dagger}}{dx}\left(\frac{d\theta}{dx} + \frac{d\hat{G}^a}{dx}\frac{\sigma^a}{2}\right)\Phi_i^0 + \text{h.c.}\right]\end{aligned} \tag{6.8}$$

6.1 Goldstone bosons

If we consider the case where only one of the $\hat{G}^a$ is non-zero, we can obtain a simpler set of equations for the Goldstone bosons $\hat{G}^a$ using the energy density given in equation (6.8):

$$\frac{d}{dx}\left(\frac{1}{2}|\Phi_i^0|^2\frac{d\hat{G}^a}{dx} + \Phi_i^{0\dagger}\sigma^a\Phi_i^0\frac{d\theta}{dx} + \left(\frac{i}{2}\frac{d\Phi_i^{0\dagger}}{dx}\sigma^a\Phi_i^0 + \text{h.c.}\right)\right) = 0 \tag{6.9}$$

The equation implies that the terms inside the derivative is a constant, and the constant is zero if we assume that all spatial derivatives vanish at infinities. Therefore we have the following equation of motion for $\hat{G}^a$:

$$\frac{1}{2}|\Phi_i^0|^2\frac{d\hat{G}^a}{dx} + \Phi_i^{0\dagger}\sigma^a\Phi_i^0\frac{d\theta}{dx} + \left(\frac{i}{2}\frac{d\Phi_i^{0\dagger}}{dx}\sigma^a\Phi_i^0 + \text{h.c.}\right) = 0 \tag{6.10}$$

We can derive a similar equation of motion for $\theta(x)$ as follows:

$$2|\Phi_i^0|^2\frac{d\theta}{dx} + \Phi_i^{0\dagger}\sigma^a\Phi_i^0\frac{d\hat{G}^a}{dx} + \left(i\frac{d\Phi_i^{0\dagger}}{dx}\Phi_i^0 + \text{h.c.}\right) = 0 \tag{6.11}$$

We will use the gradient flow technique to obtain numerical solutions to the different cases with only one $\hat{G}^a$. In all our simulations, we use the physical parameters $M_H = M_A = M_{H^\pm} = 200\,\text{GeV}$, $\tan\beta = 0.85$, and $\cos(\alpha-\beta) = 1.0$.

6.1.1 Goldstone boson $\theta(x)$

We will first consider the case where $\hat{G}^1(x), \hat{G}^2(x), \hat{G}^3(x) = 0$ for all x. This means that the matrix generating rotation of the vacua in equation (6.3) is simply $U = e^{i\theta(x)}$. In this case, the kinetic energy density of the system will become the following:

$$\mathcal{E}_{\text{kin}} = \frac{1}{2}\left(\frac{dv_1}{dx}\right)^2 + \frac{1}{2}\left(\frac{dv_2}{dx}\right)^2 + \frac{1}{2}\left(\frac{dv_+}{dx}\right)^2 + \frac{1}{2}v_2^2\left(\frac{d\xi}{dx}\right)^2 + \frac{1}{2}(v_1^2 + v_2^2 + v_+^2)\left(\frac{d\theta}{dx}\right)^2 + v_2^2\frac{d\xi}{dx}\frac{d\theta}{dx} \tag{6.12}$$

The gradient flow equations for v_1, v_2, ξ, v_+ and θ are derived to be the following:

$$\frac{\partial v_1}{\partial t} = \frac{\partial^2 v_1}{\partial x^2} - v_1\left(\frac{\partial\theta}{\partial x}\right)^2 + \mu_1^2 v_1 - \lambda_1 v_1^3 - \frac{1}{2}\lambda_3 v_1 v_+^2 - \frac{1}{2}(\lambda_{34} - |\lambda_5|c_{2\xi})v_1 v_2^2 \tag{6.13}$$

$$\frac{\partial v_2}{\partial t} = \frac{\partial^2 v_2}{\partial x^2} - v_2\left[\left(\frac{\partial\xi}{\partial x}\right)^2 + \left(\frac{\partial\theta}{\partial x}\right)^2 + 2\frac{\partial\xi}{\partial x}\frac{\partial\theta}{\partial x}\right] + \mu_2^2 v_2 - \lambda_2 v_2(v_2^2 + v_+^2) - \frac{1}{2}(\lambda_{34} - |\lambda_5|c_{2\xi})v_1^2 v_2 \tag{6.14}$$

$$\frac{\partial v_+}{\partial t} = \frac{\partial^2 v_+}{\partial x^2} - v_+\left(\frac{\partial\theta}{\partial x}\right)^2 + \mu_2^2 v_+ - \lambda_2 v_+(v_2^2 + v_+^2) - \frac{1}{2}\lambda_3 v_1^2 v_+ \tag{6.15}$$

$$\frac{\partial\xi}{\partial t} = v_2^2\left(\frac{\partial^2\xi}{\partial x^2} + \frac{\partial^2\theta}{\partial x^2}\right) + 2v_2\frac{\partial v_2}{\partial x}\left(\frac{\partial\xi}{\partial x} + \frac{\partial\theta}{\partial x}\right) - \frac{1}{2}|\lambda_5|v_1^2 v_2^2 s_{2\xi} \tag{6.16}$$

$$\frac{\partial\theta}{\partial t} = (v_1^2 + v_2^2 + v_+^2)\left(\frac{\partial^2\theta}{\partial x^2}\right) + v_2^2\frac{\partial^2\xi}{\partial x^2} + 2\frac{\partial\theta}{\partial x}\left(v_1\frac{\partial v_1}{\partial x} + v_2\frac{\partial v_2}{\partial x} + v_+\frac{\partial v_+}{\partial x}\right) + 2v_2\frac{\partial v_2}{\partial x}\frac{\partial\xi}{\partial x} \tag{6.17}$$

Assuming the derivatives of all Goldstone bosons and vacuum parameters tend to zero at the boundaries, in the ground state equation (6.17) would become the following equation of motion for $\theta(x)$:

$$\begin{aligned}(v_1^2 + v_2^2 + v_+^2)\frac{\partial\theta}{\partial x} + v_2^2\frac{\partial\xi}{\partial x} &= 0 \\ \Rightarrow \frac{\partial\theta}{\partial x} &= -\frac{v_2^2}{v_1^2 + v_2^2 + v_+^2}\frac{\partial\xi}{\partial x}\end{aligned} \tag{6.18}$$

We first impose symmetric boundary conditions such that $\theta(x) = \frac{\pi}{2}$ at both the left hand (LH) and right hand (RH) boundaries. The result of the gradient flow simulation of the five parameters is shown in Figure 6.1(a), with the corresponding R-space profiles shown in Figure 6.1(b).

The solution in Figure 6.1(a) is not charge-violating, since we can see that $v_+(x)$ is zero for all x. We can also see in Figure 6.1(b) that $R_\mu R^\mu = 0$, which again indicates the neutral vacuum condition is satisfied.

We then impose asymmetric boundary conditions $\theta = 0$ at the LH boundary and $\theta = \frac{\pi}{2}$ at the RH boundary. This corresponds to a relative rotation of the vacua. The initial guess of $\theta(x)$ was chosen to be a straight line. The gradient flow result is shown in Figure 6.1(c), with the corresponding R-space profiles shown in Figure 6.1(d). It is found that applying asymmetric boundary conditions for $\theta(x)$ does not lead to violation of the neutral vacuum condition, as seen from the zero $v_+(x)$ for all x. However, we observe non-zero $\xi(x)$ close to the kink, which leads to a non-zero R^2 component in the R-space profile. This implies that the kink solution is CP-violating. We also observe that the ground state solution for $\theta(\hat{x})$ tends asymptotically to a straight line with slope $\frac{\pi}{L}$ at the boundaries, where $L = 40$ is the range of x used in the gradient flow. In a real system $L \to \infty$, since we only truncated the x interval for the purpose of the numerical simulations. Hence in the real system we would have $\frac{\partial\theta}{\partial x} \to 0$ at the spatial infinities, as expected.

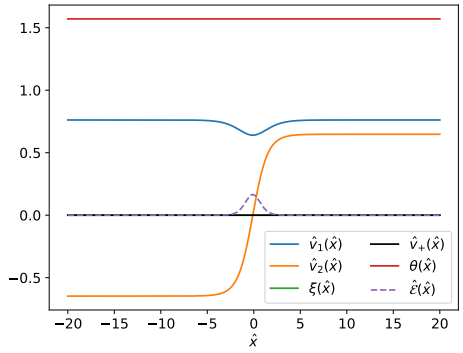

(a) Gradient flow result with $\theta(\hat{x}) = \frac{\pi}{2}$ at both boundaries.

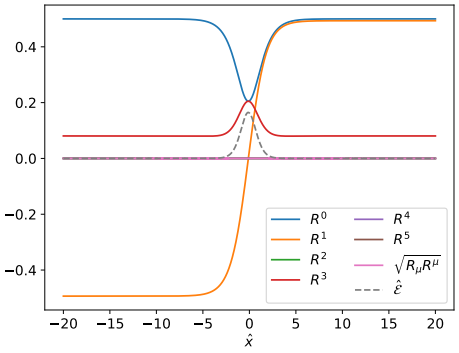

(b) R-space profiles with $\theta(\hat{x}) = \frac{\pi}{2}$ at both boundaries.

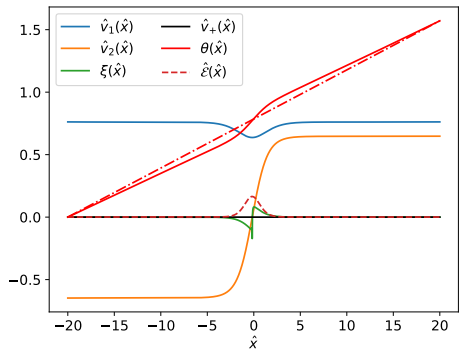

(c) Gradient flow result with $\theta(\hat{x}) = 0$ at the LH boundary and $\theta(\hat{x}) = \frac{\pi}{2}$ at the RH boundary. The dash-dotted line is a straight line between the boundary points for comparison.

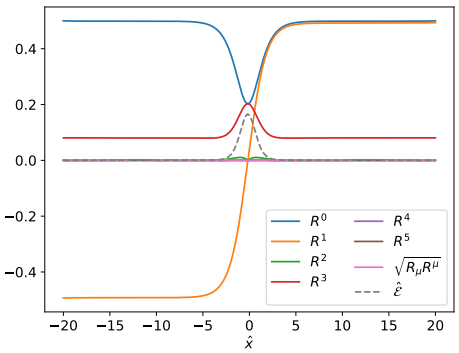

(d) R space profiles with $\theta(\hat{x}) = 0$ at the LH boundary and $\theta(\hat{x}) = \frac{\pi}{2}$ at the RH boundary.

Figure 6.1: Using gradient flow to solve for $\theta(\hat{x})$ with symmetric and asymmetric boundary conditions respectively. The two cases are $\theta = \frac{\pi}{2}$ at both boundaries, and $\theta = 0$ at the LH boundary and $\theta = \frac{\pi}{2}$ at the RH boundary respectively. Both solutions are not charge-violating, but the solution is CP-violating when asymmetric boundary conditions are applied, as evidenced by the non-zero $\xi(x)$ close to the origin.

6.1.2 Goldstone boson $\hat{G}^1(x)$

If we have $\theta(x), \hat{G}^2(x), \hat{G}^3(x) = 0$ for all x, the electroweak gauge transformation matrix will become

$$U = \exp\left(\frac{i\hat{G}^1\sigma^1}{2}\right) = \begin{pmatrix} \cos\left(\frac{\hat{G}^1}{2}\right) & i\sin\left(\frac{\hat{G}^1}{2}\right) \\ i\sin\left(\frac{\hat{G}^1}{2}\right) & \cos\left(\frac{\hat{G}^1}{2}\right) \end{pmatrix} \tag{6.19}$$

Substituting (6.19) back into (6.8), the kinetic energy density is simplified to be

$$\begin{aligned}\mathcal{E}_{\text{kin}} =& \frac{1}{2}\left(\frac{dv_1}{dx}\right)^2 + \frac{1}{2}\left(\frac{dv_2}{dx}\right)^2 + \frac{1}{2}\left(\frac{dv_+}{dx}\right)^2 + \frac{1}{2}v_2^2\left(\frac{d\xi}{dx}\right)^2 + \frac{1}{8}(v_1^2+v_2^2+v_+^2)\left(\frac{d\hat{G}^1}{dx}\right)^2 \\ &+ \frac{1}{2}\left(v_+\sin\xi\frac{dv_2}{dx} + v_+v_2\cos\xi\frac{d\xi}{dx} - v_2\sin\xi\frac{dv_+}{dx}\right)\frac{d\hat{G}^1}{dx}\end{aligned} \tag{6.20}$$

The gradient flow equations are derived to be the following:

$$\frac{\partial v_1}{\partial t} = \frac{\partial^2 v_1}{\partial x^2} - \frac{1}{4}v_1\left(\frac{\partial\hat{G}^1}{\partial x}\right)^2 + \mu_1^2 v_1 - \lambda_1 v_1^3 - \frac{1}{2}\lambda_3 v_1 v_+^2 - \frac{1}{2}(\lambda_{34} - |\lambda_5|c_{2\xi})v_1 v_2^2 \tag{6.21}$$

$$\begin{aligned}\frac{\partial v_2}{\partial t} =& \frac{\partial^2 v_2}{\partial x^2} + \frac{1}{2}v_+\sin\xi\frac{\partial^2\hat{G}^1}{\partial x^2} - v_2\left(\frac{\partial\xi}{\partial x}\right)^2 - \frac{1}{4}v_2\left(\frac{\partial\hat{G}^1}{\partial x}\right)^2 + \sin\xi\frac{\partial\hat{G}^1}{\partial x}\frac{\partial v_+}{\partial x} \\ &+ \mu_2^2 v_2 - \lambda_2 v_2(v_2^2+v_+^2) - \frac{1}{2}(\lambda_{34} - |\lambda_5|c_{2\xi})v_1^2 v_2\end{aligned} \tag{6.22}$$

$$\begin{aligned}\frac{\partial v_+}{\partial t} =& \frac{\partial^2 v_+}{\partial x^2} - \frac{1}{2}v_2\sin\xi\frac{\partial^2\hat{G}^1}{\partial x^2} - \frac{1}{4}v_+\left(\frac{\partial\hat{G}^1}{\partial x}\right)^2 - \sin\xi\frac{\partial\hat{G}^1}{\partial x}\frac{\partial v_2}{\partial x} - v_2\cos\xi\frac{\partial\hat{G}^1}{\partial x}\frac{\partial\xi}{\partial x} \\ &+ \mu_2^2 v_+ - \lambda_2 v_+(v_2^2+v_+^2) - \frac{1}{2}\lambda_3 v_1^2 v_+\end{aligned} \tag{6.23}$$

$$\frac{\partial\xi}{\partial t} = v_2^2\frac{\partial^2\xi}{\partial x^2} + 2v_2\frac{\partial v_2}{\partial x}\frac{\partial\xi}{\partial x} + \frac{1}{2}v_+v_2\cos\xi\frac{\partial^2\hat{G}^1}{\partial x^2} + v_2\cos\xi\frac{\partial v_+}{\partial x}\frac{\partial\hat{G}^1}{\partial x} - \frac{1}{2}|\lambda_5|v_1^2v_2^2s_{2\xi} \tag{6.24}$$

$$\begin{aligned}\frac{\partial \hat{G}^1}{\partial t} =& \frac{1}{4}(v_1^2 + v_2^2 + v_+^2)\frac{\partial^2 \hat{G}^1}{\partial x^2} + \frac{\partial}{\partial x}\left(\frac{1}{2}v_+ \sin\xi \frac{\partial v_2}{\partial x} + \frac{1}{2}v_+ v_2 \cos\xi \frac{\partial \xi}{\partial x} - \frac{1}{2}v_2 \sin\xi \frac{\partial v_+}{\partial x}\right) \\ &+ \frac{1}{2}\left(v_1 \frac{\partial v_1}{\partial x} + v_2 \frac{\partial v_2}{\partial x} + v_+ \frac{\partial v_+}{\partial x}\right)\left(\frac{\partial \hat{G}^1}{\partial x}\right)\end{aligned} \tag{6.25}$$

Assuming the derivatives of all Goldstone bosons and vacuum parameters tend to zero at the boundaries, in the ground state equation (6.25) would become the following equation of motion for $\hat{G}^1$:

$$\begin{aligned}\frac{1}{4}(v_1^2 + v_2^2 + v_+^2)\frac{\partial \hat{G}^1}{\partial x} - \frac{1}{2}v_2^2 \sin^2\xi \frac{\partial}{\partial x}\left(\frac{v_+}{v_2 \sin\xi}\right) = 0 \\ \Rightarrow \frac{\partial \hat{G}^1}{\partial x} = \frac{2v_2^2 \sin^2\xi}{v_1^2 + v_2^2 + v_+^2}\frac{\partial}{\partial x}\left(\frac{v_+}{v_2 \sin\xi}\right)\end{aligned} \tag{6.26}$$

From equation (6.26), we can see that when $\sin\xi(x) \neq 0$ and $\frac{\partial \hat{G}^1(x)}{\partial x} \neq 0$ for some x, then $v_+(x) \neq 0$.

The results of the gradient flow are shown in Figure 6.2. Figure 6.2(a) shows the result using the boundary conditions $\hat{G}^1 = \frac{\pi}{2}$ at both the LH and RH boundaries, with the corresponding profiles in the linear parametrization shown in Figure 6.2(b). Figure 6.2(c) shows the result obtained by imposing $\hat{G}^1 = 0$ at the LH boundary and $\hat{G}^1 = \frac{\pi}{2}$ at the RH boundary, with the corresponding profiles in the linear parametrization shown in Figure 6.2(d). Similar to $\theta(x)$, no charge violation is observed for both sets of boundary conditions used for $\hat{G}^1$. When asymmetric boundary conditions are used, the solution for $\hat{G}^1$ tends asymptotically to a straight line with slope $\frac{\pi}{L}$, where $L = 40$ is the range of x used in the simulation. As before, this agrees with our expectation that $\frac{\partial \hat{G}^1}{\partial x} \to 0$ at the spatial infinities, i.e when $L \to \infty$.

The profiles in the linear parametrization are shown in Figures 6.2(b) and 6.2(d). When symmetric boundary conditions are used for $\hat{G}^1(x)$, the ground state solu-

tion gives a constant $\hat{G}^1(x)$ across all x. However, when asymmetric boundary conditions are used, the resultant solution of $\hat{G}^1(x)$ varies with x. This leads to a relative rotation of the vacuum parameters across different values of x. The linear parametrization profiles shown in Figure 6.2(d) demonstrates this effect.

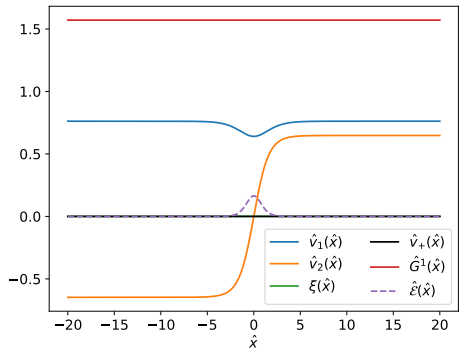

(a) Gradient flow result with $\hat{G}^1(\hat{x}) = \frac{\pi}{2}$ at both boundaries.

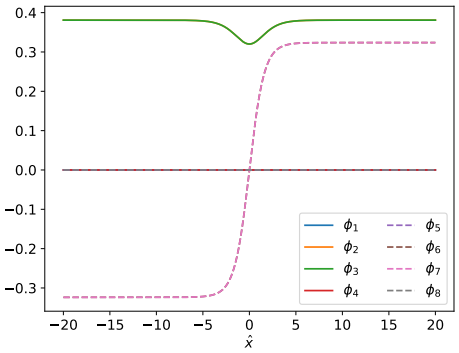

(b) Profiles in the linear parametrization with $\hat{G}^1(\hat{x}) = \frac{\pi}{2}$ at both boundaries.

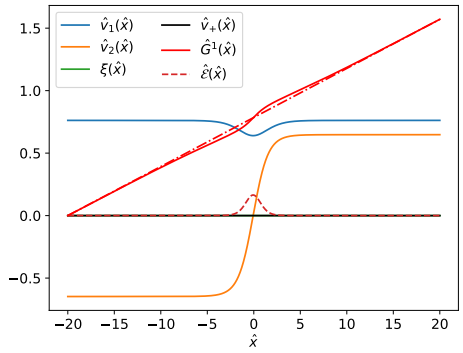

(c) Gradient flow result with $\hat{G}^1(\hat{x}) = 0$ at the LH boundary and $\hat{G}^1(\hat{x}) = \frac{\pi}{2}$ at the RH boundary. The dash-dotted line is a straight line between the boundary points for comparison.

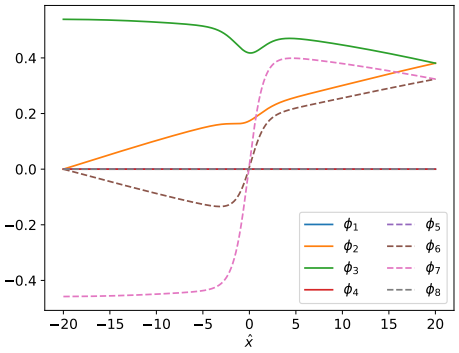

(d) Profiles in the linear parametrization with $\hat{G}^1(\hat{x}) = 0$ at the LH boundary and $\hat{G}^1(\hat{x}) = \frac{\pi}{2}$ at the RH boundary.

Figure 6.2: Using gradient flow to solve for $\hat{G}^1(\hat{x})$ with symmetric and asymmetric boundary conditions respectively. The two cases are $\hat{G}^1 = \frac{\pi}{2}$ at both boundaries, and $\hat{G}^1 = 0$ at the LH boundary and $\hat{G}^1 = \frac{\pi}{2}$ at the RH boundary respectively. Both solutions are not charge-violating.

6.1.3 Goldstone boson $\hat{G}^2(x)$

If we have $\theta(x), \hat{G}^1(x), \hat{G}^3(x) = 0$ for all x, the electroweak gauge transformation matrix will become $U = \exp(\frac{i\hat{G}^2\sigma^2}{2})$. Then the kinetic energy density becomes

$$\begin{aligned}\mathcal{E}_{\text{kin}} =&\frac{1}{2}\left(\frac{dv_1}{dx}\right)^2 + \frac{1}{2}\left(\frac{dv_2}{dx}\right)^2 + \frac{1}{2}\left(\frac{dv_+}{dx}\right)^2 + \frac{1}{2}v_2^2\left(\frac{d\xi}{dx}\right)^2 + \frac{1}{8}(v_1^2+v_2^2+v_+^2)\left(\frac{d\hat{G}^2}{dx}\right)^2 \\ &+ \frac{1}{2}\left(v_2\cos\xi\frac{dv_+}{dx} - v_+\cos\xi\frac{dv_2}{dx} + v_2v_+\sin\xi\frac{d\xi}{dx}\right)\frac{d\hat{G}^2}{dx}\end{aligned} \tag{6.27}$$

The gradient flow equations can be derived to be the following:

$$\frac{\partial v_1}{\partial t} = \frac{\partial^2 v_1}{\partial x^2} - \frac{1}{4}v_1\left(\frac{\partial\hat{G}^2}{\partial x}\right)^2 + \mu_1^2 v_1 - \lambda_1 v_1^3 - \frac{1}{2}\lambda_3 v_1 v_+^2 - \frac{1}{2}(\lambda_{34} - |\lambda_5|c_{2\xi})v_1v_2^2 \tag{6.28}$$

$$\begin{aligned}\frac{\partial v_2}{\partial t} =&\frac{\partial^2 v_2}{\partial x^2} - v_2\left(\frac{\partial\xi}{\partial x}\right)^2 - \frac{1}{2}v_+\cos\xi\frac{\partial^2\hat{G}^2}{\partial x^2} - \frac{1}{4}v_2\left(\frac{\partial\hat{G}^2}{\partial x}\right)^2 - \cos\xi\frac{\partial v_+}{\partial x}\frac{\partial\hat{G}^2}{\partial x} \\ &+ \mu_2^2 v_2 - \lambda_2 v_2(v_2^2+v_+^2) - \frac{1}{2}(\lambda_{34} - |\lambda_5|c_{2\xi})v_1^2v_2\end{aligned} \tag{6.29}$$

$$\begin{aligned}\frac{\partial v_+}{\partial t} =&\frac{\partial^2 v_+}{\partial x^2} + \frac{1}{2}v_2\cos\xi\frac{\partial^2\hat{G}^2}{\partial x^2} - \frac{1}{4}v_+\left(\frac{\partial\hat{G}^2}{\partial x}\right)^2 + \cos\xi\frac{\partial v_2}{\partial x}\frac{\partial\hat{G}^2}{\partial x} - v_2\sin\xi\frac{\partial\xi}{\partial x}\frac{\partial\hat{G}^2}{\partial x} \\ &+ \mu_2^2 v_+ - \lambda_2 v_+(v_2^2+v_+^2) - \frac{1}{2}\lambda_3 v_1^2 v_+\end{aligned} \tag{6.30}$$

$$\frac{\partial\xi}{\partial t} = v_2^2\frac{\partial^2\xi}{\partial x^2} + \frac{1}{2}v_2v_+\sin\xi\frac{\partial^2\hat{G}^2}{\partial x^2} + 2v_2\frac{\partial v_2}{\partial x}\frac{\partial\xi}{\partial x} + v_2\sin\xi\frac{\partial v_+}{\partial x}\frac{\partial\hat{G}^2}{\partial x} - \frac{1}{2}|\lambda_5|v_1^2v_2^2s_{2\xi} \tag{6.31}$$

$$\begin{aligned}\frac{\partial\hat{G}^2}{\partial t} =&\frac{1}{4}(v_1^2+v_2^2+v_+^2)\frac{\partial^2\hat{G}^2}{\partial x^2} + \frac{1}{2}\left(v_1\frac{\partial v_1}{\partial x} + v_2\frac{\partial v_2}{\partial x} + v_+\frac{\partial v_+}{\partial x}\right)\left(\frac{\partial\hat{G}^2}{\partial x}\right) \\ &+ \frac{1}{2}\frac{\partial}{\partial x}\left(v_2\cos\xi\frac{\partial v_+}{\partial x} - v_+\cos\xi\frac{\partial v_2}{\partial x} + v_2v_+\sin\xi\frac{\partial\xi}{\partial x}\right)\end{aligned} \tag{6.32}$$

The equation of motion for $\hat{G}^2(x)$ can be deduced by looking at equation (6.32) in the ground state:

$$\begin{aligned} \frac{1}{4}(v_1^2 + v_2^2 + v_+^2)\frac{\partial \hat{G}^2}{\partial x} + \frac{v_2^2 \cos^2\xi}{2}\frac{\partial}{\partial x}\left(\frac{v_+}{v_2 \cos\xi}\right) = 0 \\ \Rightarrow \frac{\partial \hat{G}^2}{\partial x} = -\frac{2v_2^2 \cos^2\xi}{v_1^2 + v_2^2 + v_+^2}\frac{\partial}{\partial x}\left(\frac{v_+}{v_2 \cos\xi}\right) \end{aligned} \tag{6.33}$$

We investigate three different cases, one where $\hat{G}^2$ is set to $\frac{\pi}{2}$ at both boundaries (shown in Figures 6.3(a) and 6.3(b)), one where there is a relative rotation of $\hat{G}^2 = \frac{\pi}{2}$ at the RH boundary (shown in Figures 6.3(c) and 6.3(d)), and one where there is a relative rotation of $\hat{G}^2 = \pi$ at the RH boundary (shown in Figures 6.3(e) and 6.3(f)).

The solution is not charge-violating when $\hat{G}^2$ is set to $\frac{\pi}{2}$ at both boundaries, as seen from $v_+(x)$ being zero across all values of x. This case corresponds to a uniform rotation of the vacuum parameters across all x. We observe local charge violation in the results where there is a relative rotation of $\hat{G}^2 = \frac{\pi}{2}$ and $\hat{G}^2 = \pi$ at the RH boundary respectively, as seen from the non-zero v_+ close to the kink at the origin. This agrees with the result presented in [31] where a peak in v_+ was observed when a relative rotation of $\frac{\pi}{2}$ was applied to γ_1 at the right hand boundary. Note that applying non-zero γ_1 is equivalent to applying a non-zero $\hat{G}^2$ here as long as all the other electroweak group parameters are set to zero. More explicitly, we have

$$U = \exp\left(\frac{i\hat{G}^2\sigma^2}{2}\right) = \begin{pmatrix} \cos\left(\frac{\hat{G}^2}{2}\right) & \sin\left(\frac{\hat{G}^2}{2}\right) \\ -\sin\left(\frac{\hat{G}^2}{2}\right) & \cos\left(\frac{\hat{G}^2}{2}\right) \end{pmatrix} \ , \tag{6.34}$$

which is the same expression as (2.26) in [31] with $\gamma_1 = \frac{\hat{G}^2}{2}$, $\gamma_2 = \gamma_3 = \theta = 0$. However, in this analysis the full profile of $\hat{G}^2$ is determined using the gradient flow technique, instead of only applying a non-zero $\hat{G}^2$ at the RH boundary.

For the case with symmetric boundary conditions, we observe no charge violation in the solution. Also, the energy of the system is found to be 0.354, which is same as the energy without applying the Goldstone mode. This is because $\hat{G}^2(\hat{x})$ is flat

in the ground state solution, and does not contribute to the energy density shown in (6.27).

It is found that applying asymmetric boundary conditions to $\hat{G}^2$ leads to charge-violating kink solutions. For the case with a relative rotation of $\frac{\pi}{2}$ at the RH boundary, which is shown in Figure 6.3(c), the peak in v_+ is 0.047. Charge violation is also evident from the non-zero $R_\mu R^\mu$ shown in Figure 6.3(d). The maximum $R_\mu R^\mu$ is found to be 0.00090. If we impose $\hat{G}^2(\hat{x}) = \pi$ at the RH boundary, for which the results are shown in Figure 6.3(e) and 6.3(f), the peak value of v_+ becomes 0.089, and the maximum value of $R_\mu R^\mu$ becomes 0.0032. This implies that a large charge-violating effect can be achieved by increasing the relative rotation of the vacuum at the RH boundary. This agrees with the result presented in Figure 10 of [31], with $\max(R_\mu R^\mu)$ increasing with increasing γ_1 applied at the RH boundary.

It is also noted that $\sqrt{R_\mu R^\mu} = |R^4|$. Since both $\xi(x)$ and $\theta(x)$ are zero for all x, referring to the components of R^μ in terms of the vacuum parameters shown in (4.18), it can be shown that $\sqrt{R_\mu R^\mu} = \sqrt{(R^0)^2 - (R^1)^2 - (R^2)^2 - (R^3)^2} = 2v_1 v_+ = |R^4|$. This relation is satisfied in our R-space profiles shown in Figures 6.3(d) and 6.3(f).

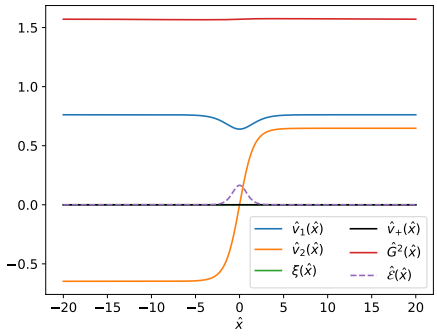

(a) Gradient flow result with $\hat{G}^2(\hat{x}) = \frac{\pi}{2}$ at both boundaries.

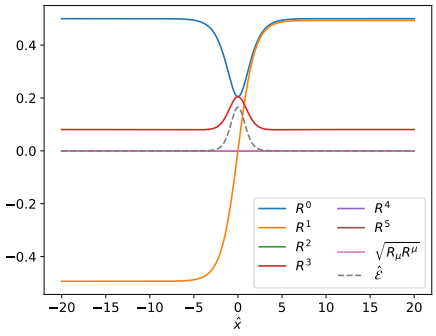

(b) R-space profiles with $\hat{G}^2(\hat{x}) = \frac{\pi}{2}$ at both boundaries.

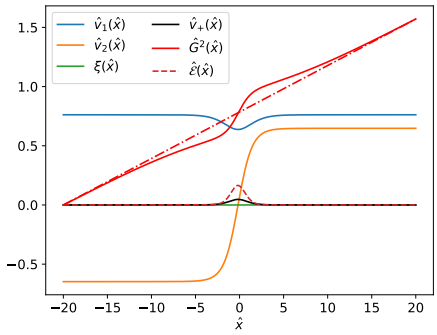

(c) Gradient flow result with $\hat{G}^2(\hat{x}) = 0$ at the LH boundary and $\hat{G}^2(\hat{x}) = \frac{\pi}{2}$ at the RH boundary.

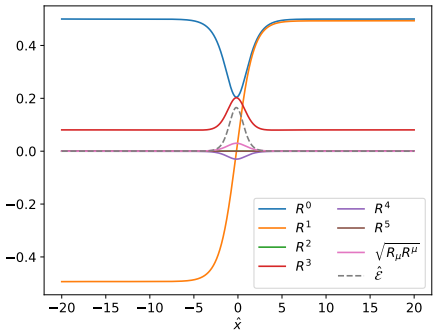

(d) R-space profiles with $\hat{G}^2(\hat{x}) = 0$ at the LH boundary and $\hat{G}^2(\hat{x}) = \frac{\pi}{2}$ at the RH boundary.

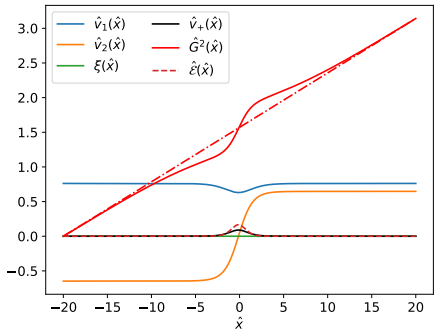

(e) Gradient flow result with $\hat{G}^2(\hat{x}) = 0$ at the LH boundary and $\hat{G}^2(\hat{x}) = \pi$ at the RH boundary.

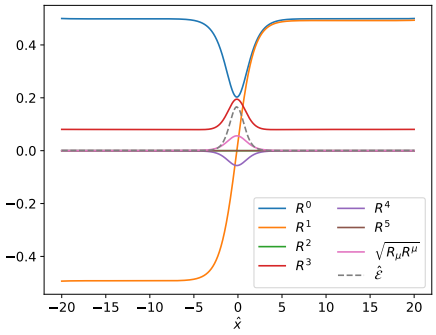

(f) R-space profiles with $\hat{G}^2(\hat{x}) = 0$ at the LH boundary and $\hat{G}^2(\hat{x}) = \pi$ at the RH boundary.

Figure 6.3: Using gradient flow to solve for $\hat{G}^2(\hat{x})$ with symmetric and asymmetric boundary conditions respectively. Charge violation is observed locally for the cases with asymmetric boundary conditions, as evidenced by the non-zero v_+ and non-zero $R_\mu R^\mu$ near the kink.

6.1.4 Goldstone boson $\hat{G}^3(x)$

If we have $\theta(x), \hat{G}^1(x), \hat{G}^2(x) = 0$ for all x, the electroweak gauge transformation matrix will be given by

$$U = \exp\left(\frac{i\hat{G}^3\sigma^3}{2}\right) = \begin{pmatrix} e^{\frac{i\hat{G}^3}{2}} & 0 \\ 0 & e^{-\frac{i\hat{G}^3}{2}} \end{pmatrix} \tag{6.35}$$

Then the kinetic energy density becomes

$$\begin{aligned}\mathcal{E}_{\text{kin}} =& \frac{1}{2}\left(\frac{dv_1}{dx}\right)^2 + \frac{1}{2}\left(\frac{dv_2}{dx}\right)^2 + \frac{1}{2}\left(\frac{dv_+}{dx}\right)^2 + \frac{1}{2}v_2^2\left(\frac{d\xi}{dx}\right)^2 + \frac{1}{8}(v_1^2+v_2^2+v_+^2)\left(\frac{d\hat{G}^3}{dx}\right)^2 \\ & - \frac{1}{2}v_2^2\frac{d\xi}{dx}\frac{d\hat{G}^3}{dx}\end{aligned} \tag{6.36}$$

The gradient flow equations can be derived to be the following:

$$\frac{\partial v_1}{\partial t} = \frac{\partial^2 v_1}{\partial x^2} - \frac{1}{4}v_1\left(\frac{\partial \hat{G}^3}{\partial x}\right)^2 + \mu_1^2 v_1 - \lambda_1 v_1^3 - \frac{1}{2}\lambda_3 v_1 v_+^2 - \frac{1}{2}(\lambda_{34} - |\lambda_5|c_{2\xi})v_1 v_2^2 \tag{6.37}$$

$$\frac{\partial v_2}{\partial t} = \frac{\partial^2 v_2}{\partial x^2} - v_2\left(\frac{\partial \xi}{\partial x}\right)^2 - \frac{1}{4}v_2\left(\frac{d\hat{G}^3}{\partial x}\right)^2 + v_2\frac{\partial \xi}{\partial x}\frac{\partial \hat{G}^3}{\partial x} + \mu_2^2 v_2 - \lambda_2 v_2(v_2^2+v_+^2) - \frac{1}{2}(\lambda_{34} - |\lambda_5|c_{2\xi})v_1^2 v_2 \tag{6.38}$$

$$\frac{\partial v_+}{\partial t} = \frac{\partial^2 v_+}{\partial x^2} - \frac{1}{4}v_+\left(\frac{\partial \hat{G}^3}{\partial x}\right)^2 + \mu_2^2 v_+ - \lambda_2 v_+(v_2^2+v_+^2) - \frac{1}{2}\lambda_3 v_1^2 v_+ \tag{6.39}$$

$$\frac{\partial \xi}{\partial t} = v_2^2\frac{\partial^2 \xi}{\partial x^2} - \frac{1}{2}v_2^2\frac{\partial^2 \hat{G}^3}{\partial x^2} + 2v_2\frac{\partial v_2}{\partial x}\frac{\partial \xi}{\partial x} - v_2\frac{\partial v_2}{\partial x}\frac{\partial \hat{G}^3}{\partial x} - \frac{1}{2}|\lambda_5|v_1^2 v_2^2 s_{2\xi} \tag{6.40}$$

$$\frac{\partial \hat{G}^3}{\partial t} = \frac{1}{4}\left(v_1^2+v_2^2+v_+^2\right)\frac{\partial^2 \hat{G}^3}{\partial x^2} - \frac{1}{2}v_2^2\frac{\partial^2 \xi}{\partial x^2} + \frac{1}{2}\left(v_1\frac{\partial v_1}{\partial x} + v_2\frac{\partial v_2}{\partial x} + v_+\frac{\partial v_+}{\partial x}\right)\frac{\partial \hat{G}^3}{\partial x} - v_2\frac{\partial v_2}{\partial x}\frac{\partial \xi}{\partial x} \tag{6.41}$$

The equation of motion for $\hat{G}^3$ can be derived by considering the ground state of equation (6.41):

$$\begin{aligned} \frac{1}{4}\left(v_1^2+v_2^2+v_+^2\right)\frac{\partial \hat{G}^3}{\partial x}-\frac{1}{2}v_2^2\frac{\partial \xi}{\partial x}=0 \\ \Rightarrow \frac{\partial \hat{G}^3}{\partial x}=\frac{2v_2^2}{v_1^2+v_2^2+v_+^2}\frac{\partial \xi}{\partial x} \end{aligned} \tag{6.42}$$

The gradient flow results are shown in Figure 6.4. Figure 6.4(a) shows the result using the boundary conditions $\hat{G}^3=\frac{\pi}{2}$ at both the LH and RH boundaries, with the corresponding profiles in the linear parametrization shown in Figure 6.4(b). Figure 6.4(c) shows the result obtained by imposing $\hat{G}^3=0$ at the LH boundary and $\hat{G}^3=\frac{\pi}{2}$ at the RH boundary, with the corresponding profiles in the linear parametrization shown in Figure 6.4(d). Similar to $\theta(x)$ and $\hat{G}^1(x)$, no violation of the neutral vacuum condition is observed when either symmetric or asymmetric boundary conditions are applied to $\hat{G}^3$. When asymmetric boundary conditions are used, however, we observe non-zero $\xi(x)$ close to the kink at the origin, which indicates CP-violation in the kink solution.

Comparing the profiles in the linear parametrization shown in Figures 6.4(b) and 6.4(d), we can see that there is a relative rotation of the profiles when asymmetric boundary conditions are imposed on $\hat{G}^3$.

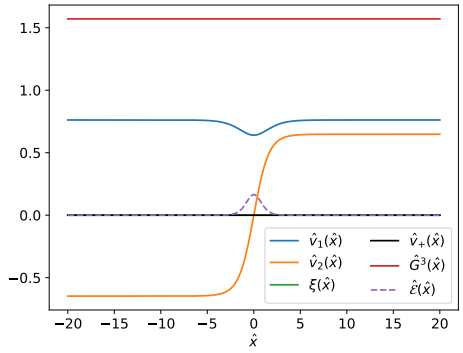

(a) Gradient flow result with $\hat{G}^3(\hat{x}) = \frac{\pi}{2}$ at both boundaries.

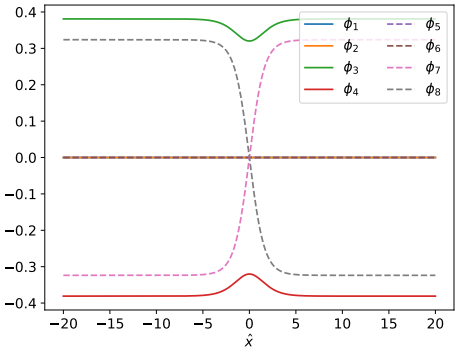

(b) Profiles in the linear parametrization with $\hat{G}^3(\hat{x}) = \frac{\pi}{2}$ at both boundaries.

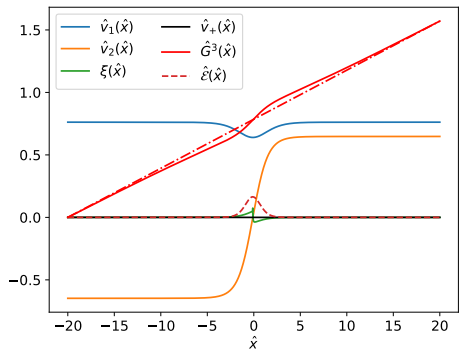

(c) Gradient flow result with $\hat{G}^3(\hat{x}) = 0$ at the LH boundary and $\hat{G}^3(\hat{x}) = \frac{\pi}{2}$ at the RH boundary. The dash-dotted line is a straight line between the boundary points for comparison.

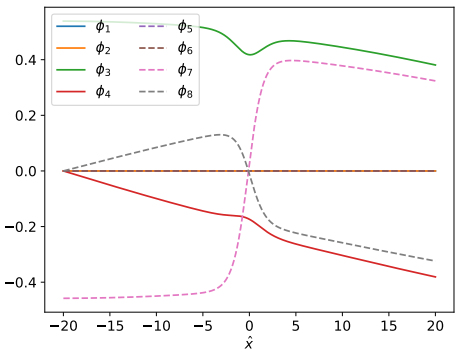

(d) Profiles in the linear parametrization with $\hat{G}^3(\hat{x}) = 0$ at the LH boundary and $\hat{G}^3(\hat{x}) = \frac{\pi}{2}$ at the RH boundary.

Figure 6.4: Using gradient flow to solve for $\hat{G}^3(\hat{x})$ with symmetric and asymmetric boundary conditions respectively. The two cases are $\hat{G}^3 = \frac{\pi}{2}$ at both boundaries, and $\hat{G}^3 = 0$ at the LH boundary and $\hat{G}^3 = \frac{\pi}{2}$ at the RH boundary respectively. Both solutions are not charge-violating, but the kink solution is CP-violating when asymmetric boundary conditions are applied, as seen from the non-zero $\xi(x)$ near the kink.

6.1.5 Goldstone bosons $\theta(x)$ and $\hat{G}^1(x)$

If we incorporate both $\theta(x)$ and $\hat{G}^1(x)$ into our simulations, which means that the $\mathrm{U}(1)\times\mathrm{SU}(2)$ matrix generating the transformation $U = e^{i\theta}e^{\frac{i\hat{G}^1\sigma^1}{2}}$, then the kinetic part of the energy density will become

$$\begin{aligned}\mathcal{E}_{\text{kin}} =&\frac{1}{2}\left(\frac{dv_1}{dx}\right)^2+\frac{1}{2}\left(\frac{dv_2}{dx}\right)^2+\frac{1}{2}\left(\frac{dv_+}{dx}\right)^2+\frac{1}{2}v_2^2\left(\frac{d\xi}{dx}\right)^2+\frac{1}{2}(v_1^2+v_2^2+v_+^2)\left[\left(\frac{d\theta}{dx}\right)^2\right.\\&\left.+\frac{1}{4}\left(\frac{d\hat{G}^1}{dx}\right)^2\right]+\frac{1}{2}\left(v_+\sin\xi\frac{dv_2}{dx}+v_+v_2\cos\xi\frac{d\xi}{dx}-v_2\sin\xi\frac{dv_+}{dx}\right)\frac{d\hat{G}^1}{dx}+v_2^2\frac{d\xi}{dx}\frac{d\theta}{dx}\\&+v_2v_+\cos\xi\frac{d\theta}{dx}\frac{d\hat{G}^1}{dx}\end{aligned} \tag{6.43}$$

The gradient flow equations are derived to be the following:

$$\frac{\partial v_1}{\partial t} = \frac{\partial^2 v_1}{\partial x^2}-v_1\left[\left(\frac{\partial\theta}{\partial x}\right)^2+\frac{1}{4}\left(\frac{\partial\hat{G}^1}{\partial x}\right)^2\right]+\mu_1^2v_1-\lambda_1v_1^3-\frac{1}{2}\lambda_3v_1v_+^2-\frac{1}{2}(\lambda_{34}-|\lambda_5|c_{2\xi})v_1v_2^2 \tag{6.44}$$

$$\begin{aligned}\frac{\partial v_2}{\partial t} =&\frac{\partial^2 v_2}{\partial x^2}-v_2\left[\left(\frac{\partial\xi}{\partial x}\right)^2+\left(\frac{\partial\theta}{\partial x}\right)^2+\frac{1}{4}\left(\frac{\partial\hat{G}^1}{\partial x}\right)^2+2\frac{\partial\xi}{\partial x}\frac{\partial\theta}{\partial x}\right]+\frac{1}{2}v_+\sin\xi\frac{\partial^2\hat{G}^1}{\partial x^2}\\&+\sin\xi\frac{\partial\hat{G}^1}{\partial x}\frac{\partial v_+}{\partial x}-v_+\cos\xi\frac{\partial\theta}{\partial x}\frac{\partial\hat{G}^1}{\partial x}+\mu_2^2v_2-\lambda_2v_2(v_2^2+v_+^2)-\frac{1}{2}(\lambda_{34}-|\lambda_5|c_{2\xi})v_1^2v_2\end{aligned} \tag{6.45}$$

$$\begin{aligned}\frac{\partial v_+}{\partial t} =&\frac{\partial^2 v_+}{\partial x^2}-v_+\left[\left(\frac{\partial\theta}{\partial x}\right)^2+\frac{1}{4}\left(\frac{\partial\hat{G}^1}{\partial x}\right)^2\right]-\frac{1}{2}v_2\sin\xi\frac{\partial^2\hat{G}^1}{\partial x^2}-\sin\xi\frac{\partial\hat{G}^1}{\partial x}\frac{\partial v_2}{\partial x}\\&-v_2\cos\xi\frac{\partial\hat{G}^1}{\partial x}\frac{\partial\xi}{\partial x}-v_2\cos\xi\frac{\partial\theta}{\partial x}\frac{\partial\hat{G}^1}{\partial x}+\mu_2^2v_+-\lambda_2v_+(v_2^2+v_+^2)-\frac{1}{2}\lambda_3v_1^2v_+\end{aligned} \tag{6.46}$$

$$\frac{\partial \xi}{\partial t} = v_2^2 \frac{\partial^2 \xi}{\partial x^2} + 2v_2 \frac{\partial v_2}{\partial x}\frac{\partial \xi}{\partial x} + \frac{1}{2}v_+ v_2 \cos\xi \frac{\partial^2 \hat{G}^1}{\partial x^2} + v_2 \cos\xi \frac{\partial v_+}{\partial x}\frac{\partial \hat{G}^1}{\partial x} + 2v_2 \frac{\partial v_2}{\partial x}\frac{\partial \theta}{\partial x} + v_2^2 \frac{\partial^2 \theta}{\partial x^2} + v_2 v_+ \sin\xi \frac{\partial \theta}{\partial x}\frac{\partial \hat{G}^1}{\partial x} - \frac{1}{2}|\lambda_5| v_1^2 v_2^2 s_{2\xi} \tag{6.47}$$

$$\frac{\partial \theta}{\partial t} = (v_1^2 + v_2^2 + v_+^2)\left(\frac{\partial^2 \theta}{\partial x^2}\right) + v_2^2 \frac{\partial^2 \xi}{\partial x^2} + v_2 v_+ \cos\xi \frac{\partial^2 \hat{G}^1}{\partial x^2} + 2\frac{\partial \theta}{\partial x}\left(v_1 \frac{\partial v_1}{\partial x} + v_2 \frac{\partial v_2}{\partial x} + v_+ \frac{\partial v_+}{\partial x}\right) + 2v_2 \frac{\partial v_2}{\partial x}\frac{\partial \xi}{\partial x} + v_+ \cos\xi \frac{\partial v_2}{\partial x}\frac{\partial \hat{G}^1}{\partial x} + v_2 \cos\xi \frac{\partial v_+}{\partial x}\frac{\partial \hat{G}^1}{\partial x} - v_2 v_+ \sin\xi \frac{\partial \xi}{\partial x}\frac{\partial \hat{G}^1}{\partial x} \tag{6.48}$$

$$\frac{\partial \hat{G}^1}{\partial t} = \frac{1}{4}(v_1^2 + v_2^2 + v_+^2)\frac{\partial^2 \hat{G}^1}{\partial x^2} + v_2 v_+ \cos\xi \frac{\partial^2 \theta}{\partial x^2} + \frac{\partial}{\partial x}\left(\frac{1}{2}v_+ \sin\xi \frac{\partial v_2}{\partial x} + \frac{1}{2}v_+ v_2 \cos\xi \frac{\partial \xi}{\partial x} - \frac{1}{2}v_2 \sin\xi \frac{\partial v_+}{\partial x}\right) + \frac{1}{2}\left(v_1 \frac{\partial v_1}{\partial x} + v_2 \frac{\partial v_2}{\partial x} + v_+ \frac{\partial v_+}{\partial x}\right)\left(\frac{\partial \hat{G}^1}{\partial x}\right) + v_+ \cos\xi \frac{\partial v_2}{\partial x}\frac{\partial \theta}{\partial x} + v_2 \cos\xi \frac{\partial v_+}{\partial x}\frac{\partial \theta}{\partial x} - v_2 v_+ \sin\xi \frac{\partial \xi}{\partial x}\frac{\partial \theta}{\partial x} \tag{6.49}$$

Asymmetric boundary conditions are applied to both θ and $\hat{G}^1$ such that $\hat{G}^1(\hat{x}) = 0$ and $\theta(\hat{x}) = 0$ at the LH boundary, while $\hat{G}^1(\hat{x}) = \frac{\pi}{2}$ and $\theta(\hat{x}) = \frac{\pi}{2}$ at the RH boundary. The gradient flow result is shown in Figure 6.5(a), with the corresponding R-space profiles shown in Figure 6.5(b). We observe no charge violation in the solution, since both v_+ and $R_\mu R^\mu$ are zero for all x.

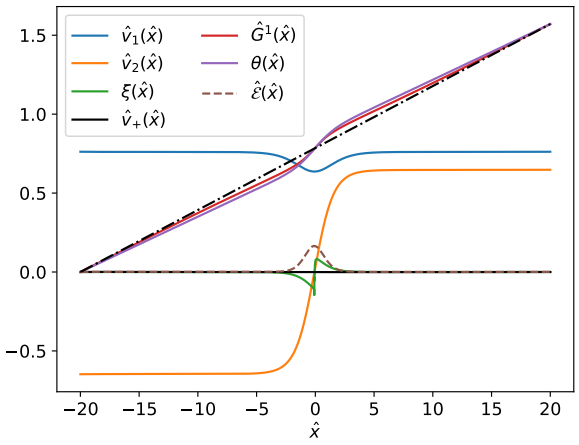

(a) Gradient flow result with $\hat{G}^1(\hat{x}) = 0$ and $\theta(\hat{x}) = 0$ at the LH boundary, $\hat{G}^1(\hat{x}) = \frac{\pi}{2}$ and $\theta(\hat{x}) = \frac{\pi}{2}$ at the RH boundary. The dash-dotted line is a straight line between the boundary points for comparison.

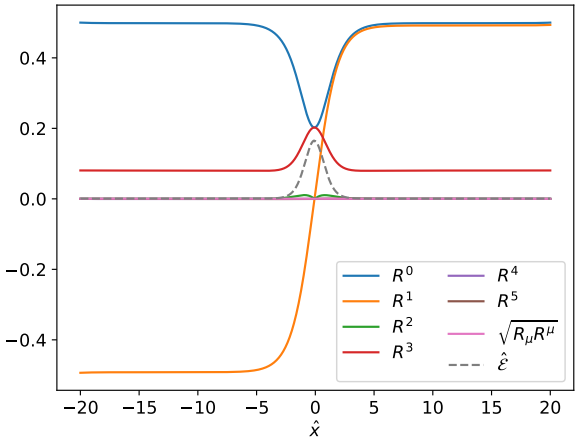

(b) R-space profiles with $\hat{G}^1(\hat{x}) = 0$ and $\theta(\hat{x}) = 0$ at the LH boundary, $\hat{G}^1(\hat{x}) = \frac{\pi}{2}$ and $\theta(\hat{x}) = \frac{\pi}{2}$ at the RH boundary.

Figure 6.5: Using gradient flow to solve for $\hat{G}^1(\hat{x})$ and $\theta(\hat{x})$, both with asymmetric boundary conditions. The solution respects the charge symmetry, but violates CP near the origin.

6.1.6 Goldstone bosons $\theta(x)$ and $\hat{G}^2(x)$

If we incorporate both $\theta(x)$ and $\hat{G}^2(x)$ into our simulations, which means that the U(1) $\times$ SU(2) matrix generating the transformation is $U = e^{i\theta}e^{\frac{i\hat{G}^2\sigma^2}{2}}$, then the kinetic part of the energy density will become

$$\begin{aligned}\mathcal{E}_{\text{kin}} =&\frac{1}{2}\left(\frac{dv_1}{dx}\right)^2 + \frac{1}{2}\left(\frac{dv_2}{dx}\right)^2 + \frac{1}{2}\left(\frac{dv_+}{dx}\right)^2 + \frac{1}{2}v_2^2\left(\frac{d\xi}{dx}\right)^2 + \frac{1}{2}(v_1^2+v_2^2+v_+^2)\left[\left(\frac{d\theta}{dx}\right)^2\right.\\ &\left.+\frac{1}{4}\left(\frac{d\hat{G}^2}{dx}\right)^2\right] + \frac{1}{2}\left(v_2\cos\xi\frac{dv_+}{dx} - v_+\cos\xi\frac{dv_2}{dx} + v_2v_+\sin\xi\frac{d\xi}{dx}\right)\frac{d\hat{G}^2}{dx} + v_2^2\frac{d\xi}{dx}\frac{d\theta}{dx}\\ &+ v_2v_+\sin\xi\frac{d\theta}{dx}\frac{d\hat{G}^2}{dx}\end{aligned} \tag{6.50}$$

The gradient flow equations are found to be

$$\frac{\partial v_1}{\partial t} = \frac{\partial^2 v_1}{\partial x^2} - v_1\left[\left(\frac{\partial\theta}{\partial x}\right)^2 + \frac{1}{4}\left(\frac{\partial\hat{G}^2}{\partial x}\right)^2\right] + \mu_1^2 v_1 - \lambda_1 v_1^3 - \frac{1}{2}\lambda_3 v_1 v_+^2 - \frac{1}{2}(\lambda_{34} - |\lambda_5|c_{2\xi})v_1 v_2^2 \tag{6.51}$$

$$\begin{aligned}\frac{\partial v_2}{\partial t} =&\frac{\partial^2 v_2}{\partial x^2} - v_2\left(\frac{\partial\xi}{\partial x}\right)^2 - v_2\left[\left(\frac{\partial\theta}{\partial x}\right)^2 + \frac{1}{4}\left(\frac{\partial\hat{G}^2}{\partial x}\right)^2\right] - \frac{1}{2}v_+\cos\xi\frac{\partial^2\hat{G}^2}{\partial x^2} - \cos\xi\frac{\partial v_+}{\partial x}\frac{\partial\hat{G}^2}{\partial x}\\ &- 2v_2\frac{\partial\xi}{\partial x}\frac{\partial\theta}{\partial x} - v_+\sin\xi\frac{\partial\theta}{\partial x}\frac{\partial\hat{G}^2}{\partial x} + \mu_2^2 v_2 - \lambda_2 v_2(v_2^2+v_+^2) - \frac{1}{2}(\lambda_{34} - |\lambda_5|c_{2\xi})v_1^2 v_2\end{aligned} \tag{6.52}$$

$$\begin{aligned}\frac{\partial v_+}{\partial t} =&\frac{\partial^2 v_+}{\partial x^2} - v_+\left[\left(\frac{\partial\theta}{\partial x}\right)^2 + \frac{1}{4}\left(\frac{\partial\hat{G}^2}{\partial x}\right)^2\right] + \frac{1}{2}v_2\cos\xi\frac{\partial^2\hat{G}^2}{\partial x^2} + \cos\xi\frac{\partial v_2}{\partial x}\frac{\partial\hat{G}^2}{\partial x} - v_2\sin\xi\frac{\partial\xi}{\partial x}\frac{\partial\hat{G}^2}{\partial x}\\ &- v_2\sin\xi\frac{\partial\theta}{\partial x}\frac{\partial\hat{G}^2}{\partial x} + \mu_2^2 v_+ - \lambda_2 v_+(v_2^2+v_+^2) - \frac{1}{2}\lambda_3 v_1^2 v_+\end{aligned} \tag{6.53}$$

$$\begin{aligned}\frac{\partial \xi}{\partial t} =& v_2^2 \frac{\partial^2 \xi}{\partial x^2} + 2v_2 \frac{\partial v_2}{\partial x}\frac{\partial \xi}{\partial x} + \frac{1}{2}v_2 v_+ \sin\xi \frac{\partial^2 \hat{G}^2}{\partial x^2} + v_2 \sin\xi \frac{\partial v_+}{\partial x}\frac{\partial \hat{G}^2}{\partial x} + 2v_2 \frac{\partial v_2}{\partial x}\frac{\partial \theta}{\partial x} + v_2^2 \frac{\partial^2 \theta}{\partial x^2} \\ & - v_2 v_+ \cos\xi \frac{\partial \theta}{\partial x}\frac{\partial \hat{G}^2}{\partial x} - \frac{1}{2}|\lambda_5| v_1^2 v_2^2 s_{2\xi}\end{aligned} \tag{6.54}$$

$$\begin{aligned}\frac{\partial \theta}{\partial t} =& (v_1^2 + v_2^2 + v_+^2)\left(\frac{\partial^2 \theta}{\partial x^2}\right) + v_2^2 \frac{\partial^2 \xi}{\partial x^2} + v_2 v_+ \sin\xi \frac{\partial^2 \hat{G}^2}{\partial x^2} + 2\frac{\partial \theta}{\partial x}\left(v_1 \frac{\partial v_1}{\partial x} + v_2 \frac{\partial v_2}{\partial x} + v_+ \frac{\partial v_+}{\partial x}\right) \\ & + 2v_2 \frac{\partial v_2}{\partial x}\frac{\partial \xi}{\partial x} + v_+ \sin\xi \frac{\partial v_2}{\partial x}\frac{\partial \hat{G}^2}{\partial x} + v_2 \sin\xi \frac{\partial v_+}{\partial x}\frac{\partial \hat{G}^2}{\partial x} + v_2 v_+ \cos\xi \frac{\partial \xi}{\partial x}\frac{\partial \hat{G}^2}{\partial x}\end{aligned} \tag{6.55}$$

$$\begin{aligned}\frac{\partial \hat{G}^2}{\partial t} =& \frac{1}{4}(v_1^2 + v_2^2 + v_+^2)\frac{\partial^2 \hat{G}^2}{\partial x^2} + \frac{1}{2}\left(v_1 \frac{\partial v_1}{\partial x} + v_2 \frac{\partial v_2}{\partial x} + v_+ \frac{\partial v_+}{\partial x}\right)\left(\frac{\partial \hat{G}^2}{\partial x}\right) \\ & + \frac{1}{2}\frac{\partial}{\partial x}\left(v_2 \cos\xi \frac{\partial v_+}{\partial x} - v_+ \cos\xi \frac{\partial v_2}{\partial x} + v_2 v_+ \sin\xi \frac{\partial \xi}{\partial x} + 2v_2 v_+ \sin\xi \frac{\partial \theta}{\partial x}\right)\end{aligned} \tag{6.56}$$

Note that the expressions on the right hand side of equations (6.55) and (6.56) can also be written in terms of total derivatives, reflecting the shift symmetry in the Goldstone bosons:

$$\frac{\partial \theta}{\partial t} = \frac{\partial}{\partial x}\left[\left(v_1^2 + v_2^2 + v_+^2\right)\frac{\partial \theta}{\partial x} + v_2^2 \frac{\partial \xi}{\partial x} + v_2 v_+ \sin\xi \frac{\partial \hat{G}^2}{\partial x}\right] \tag{6.57}$$

$$\begin{aligned}\frac{\partial \hat{G}^2}{\partial t} =& \frac{\partial}{\partial x}\left[\frac{1}{4}\left(v_1^2 + v_2^2 + v_+^2\right)\frac{\partial \hat{G}^2}{\partial x} + \frac{1}{2}v_2 \cos\xi \frac{\partial v_+}{\partial x} - \frac{1}{2}v_+ \cos\xi \frac{\partial v_2}{\partial x} + \frac{1}{2}v_2 v_+ \sin\xi \frac{\partial \xi}{\partial x}\right. \\ & \left. + v_2 v_+ \sin\xi \frac{\partial \theta}{\partial x}\right]\end{aligned} \tag{6.58}$$

Asymmetric boundary conditions are imposed for both θ and $\hat{G}^2$ such that $\hat{G}^2(\hat{x}) = 0$ and $\theta(\hat{x}) = 0$ at the LH boundary, while $\hat{G}^2(\hat{x}) = \frac{\pi}{2}$ and $\theta(\hat{x}) = \frac{\pi}{2}$ at the RH boundary. The gradient flow result is shown in Figure 6.6(a), with the corresponding R-space profiles shown in Figure 6.6(b). We observe a charge-violating solution, with a larger charge-violating effect compared to the case with only $\hat{G}^2$ applied (shown in Figure 6.2(c)). The maximum v_+ is found to be 0.061, compared to 0.047 when only $\hat{G}^2$ is present. The maximum $R_\mu R^\mu$ is found to be 0.0015,

which is nearly twice of that (0.00090) when only $\hat{G}^2$ is applied.

From the R-space profiles in Figure 6.6(b), we observe that both R^4 and R^5 are non-zero near the kink. This is due to the non-zero θ we have included in this case, and the non-zero v_+ near the kink. Also, since we have ξ non-zero around the kink, we observe a non-zero R^2 in that region.

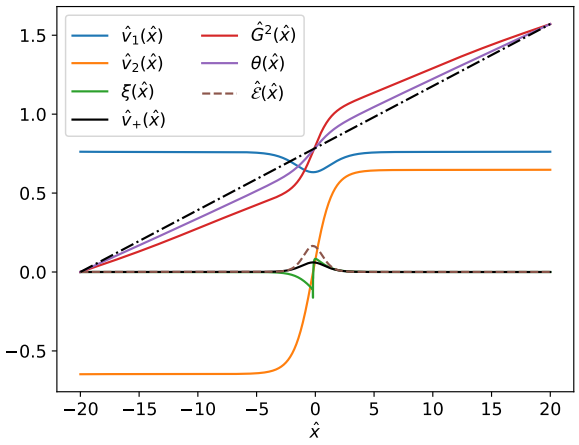

(a) Gradient flow result with $\hat{G}^2(\hat{x}) = 0$ and $\theta(\hat{x}) = 0$ at the LH boundary, $\hat{G}^2(\hat{x}) = \frac{\pi}{2}$ and $\theta(\hat{x}) = \frac{\pi}{2}$ at the RH boundary. The dash-dotted line is a straight line between the boundary points for comparison.

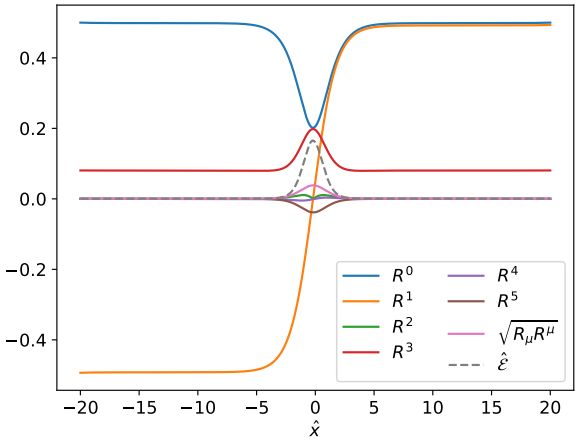

(b) R-space profiles with $\hat{G}^2(\hat{x}) = 0$ and $\theta(\hat{x}) = 0$ at the LH boundary, $\hat{G}^2(\hat{x}) = \frac{\pi}{2}$ and $\theta(\hat{x}) = \frac{\pi}{2}$ at the RH boundary.

Figure 6.6: Using gradient flow to solve for $\hat{G}^2(\hat{x})$ and $\theta(\hat{x})$, both with asymmetric boundary conditions. Charge violation can be seen from the non-zero v_+ in the plots of the vacuum parameters, and the non-zero $R_\mu R^\mu$ in the R-space profiles. CP violation is also observed from the non-zero $\xi(x)$ near the kink at the origin.

6.1.7 Goldstone bosons $\theta(x)$ and $\hat{G}^3(x)$

If we incorporate both $\theta(x)$ and $\hat{G}^3(x)$ into our simulations, which means that the U(1) $\times$ SU(2) matrix generating the transformation is $U = e^{i\theta}e^{\frac{i\hat{G}^3\sigma^3}{2}}$, then the kinetic part of the energy density will become

$$\begin{aligned}\mathcal{E}_{\text{kin}} =&\frac{1}{2}\left(\frac{dv_1}{dx}\right)^2 + \frac{1}{2}\left(\frac{dv_2}{dx}\right)^2 + \frac{1}{2}\left(\frac{dv_+}{dx}\right)^2 + \frac{1}{2}v_2^2\left(\frac{d\xi}{dx}\right)^2 + \frac{1}{2}(v_1^2+v_2^2+v_+^2)\left[\left(\frac{d\theta}{dx}\right)^2\right.\\ &\left.+\frac{1}{4}\left(\frac{d\hat{G}^3}{dx}\right)^2\right] - \frac{1}{2}v_2^2\frac{d\xi}{dx}\frac{d\hat{G}^3}{dx} + v_2^2\frac{d\xi}{dx}\frac{d\theta}{dx} + \frac{1}{2}(v_+^2 - v_1^2 - v_2^2)\frac{d\theta}{dx}\frac{d\hat{G}^3}{dx}\end{aligned} \tag{6.59}$$

The gradient flow equations are derived to be the following:

$$\begin{aligned}\frac{\partial v_1}{\partial t} =&\frac{\partial^2 v_1}{\partial x^2} - v_1\left[\left(\frac{d\theta}{dx}\right)^2 + \frac{1}{4}\left(\frac{d\hat{G}^3}{dx}\right)^2\right] + v_1\frac{\partial\theta}{dx}\frac{\partial\hat{G}^3}{dx} + \mu_1^2 v_1 - \lambda_1 v_1^3\\ &- \frac{1}{2}\lambda_3 v_1 v_+^2 - \frac{1}{2}(\lambda_{34} - |\lambda_5|c_{2\xi})v_1 v_2^2\end{aligned} \tag{6.60}$$

$$\begin{aligned}\frac{\partial v_2}{\partial t} =&\frac{\partial^2 v_2}{\partial x^2} - v_2\left(\frac{\partial\xi}{\partial x}\right)^2 - v_2\left[\left(\frac{d\theta}{dx}\right)^2 + \frac{1}{4}\left(\frac{d\hat{G}^3}{dx}\right)^2\right] + v_2\frac{\partial\xi}{\partial x}\frac{\partial\hat{G}^3}{\partial x} - 2v_2\frac{\partial\xi}{\partial x}\frac{\partial\theta}{\partial x}\\ &+ v_2\frac{\partial\theta}{\partial x}\frac{\partial\hat{G}^3}{\partial x} + \mu_2^2 v_2 - \lambda_2 v_2(v_2^2+v_+^2) - \frac{1}{2}(\lambda_{34} - |\lambda_5|c_{2\xi})v_1^2 v_2\end{aligned} \tag{6.61}$$

$$\frac{\partial v_+}{\partial t} = \frac{\partial^2 v_+}{\partial x^2} - v_+\left[\left(\frac{d\theta}{dx}\right)^2 + \frac{1}{4}\left(\frac{d\hat{G}^3}{dx}\right)^2\right] - v_+\frac{\partial\theta}{\partial x}\frac{\partial\hat{G}^3}{\partial x} + \mu_2^2 v_+ - \lambda_2 v_+(v_2^2+v_+^2) - \frac{1}{2}\lambda_3 v_1^2 v_+ \tag{6.62}$$

$$\frac{\partial\xi}{\partial t} = v_2^2\frac{\partial^2\xi}{\partial x^2} - \frac{1}{2}v_2^2\frac{\partial^2\hat{G}^3}{\partial x^2} + v_2^2\frac{\partial^2\theta}{\partial x^2} + 2v_2\frac{\partial v_2}{\partial x}\frac{\partial\xi}{\partial x} - v_2\frac{\partial v_2}{\partial x}\frac{\partial\hat{G}^3}{\partial x} + 2v_2\frac{\partial v_2}{\partial x}\frac{\partial\theta}{\partial x} - \frac{1}{2}|\lambda_5|v_1^2 v_2^2 s_{2\xi} \tag{6.63}$$

$$\frac{\partial\theta}{\partial t} =(v_1^2+v_2^2+v_+^2)\frac{\partial^2\theta}{\partial x^2}+v_2^2\frac{\partial^2\xi}{\partial x^2}+\frac{1}{2}(v_+^2-v_1^2-v_2^2)\frac{\partial^2\hat{G}^3}{\partial x^2}+2\Bigg(v_1\frac{\partial v_1}{\partial x}+v_2\frac{\partial v_2}{\partial x} + v_+\frac{\partial v_+}{\partial x}\Bigg)\frac{\partial\theta}{\partial x}+2v_2\frac{\partial v_2}{\partial x}\frac{\partial\xi}{\partial x}+\left(v_+\frac{\partial v_+}{\partial x}-v_1\frac{\partial v_1}{\partial x}-v_2\frac{\partial v_2}{\partial x}\right)\frac{\partial\hat{G}^3}{\partial x} \tag{6.64}$$

$$\frac{\partial\hat{G}^3}{\partial t} =\frac{1}{4}(v_1^2+v_2^2+v_+^2)\frac{\partial^2\hat{G}^3}{\partial x^2}-\frac{1}{2}v_2^2\frac{\partial^2\xi}{\partial x^2}+\frac{1}{2}(v_+^2-v_1^2-v_2^2)\frac{\partial^2\theta}{\partial x^2}+\frac{1}{2}\Bigg(v_1\frac{\partial v_1}{\partial x}+v_2\frac{\partial v_2}{\partial x} + v_+\frac{\partial v_+}{\partial x}\Bigg)\frac{\partial\hat{G}^3}{\partial x}-v_2\frac{\partial v_2}{\partial x}\frac{\partial\xi}{\partial x}+\left(v_+\frac{\partial v_+}{\partial x}-v_1\frac{\partial v_1}{\partial x}-v_2\frac{\partial v_2}{\partial x}\right)\frac{\partial\theta}{\partial x} \tag{6.65}$$

Asymmetric boundary conditions are applied to both θ and $\hat{G}^3$ such that $\hat{G}^3(\hat{x})=0$ and $\theta(\hat{x})=0$ at the LH boundary, while $\hat{G}^3(\hat{x})=\frac{\pi}{2}$ and $\theta(\hat{x})=\frac{\pi}{2}$ at the RH boundary. The result of the gradient simulation is shown in Figure 6.7(a), with the corresponding R-space profiles shown in Figure 6.7(b). We do not observe charge violation in the solution, since both v_+ and $R_\mu R^\mu$ are zero for all x.

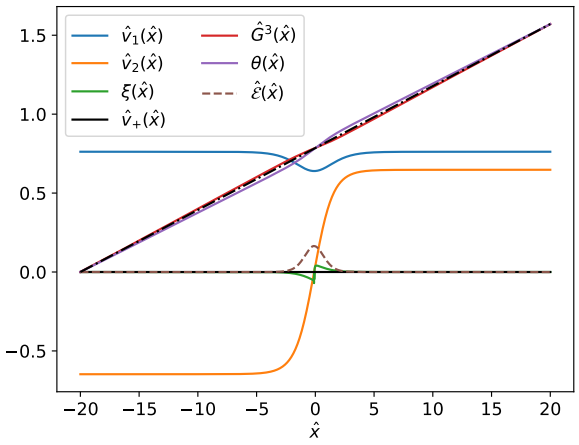

(a) Gradient flow result with $\hat{G}^3(\hat{x}) = 0$ and $\theta(\hat{x}) = 0$ at the LH boundary, $\hat{G}^3(\hat{x}) = \frac{\pi}{2}$ and $\theta(\hat{x}) = \frac{\pi}{2}$ at the RH boundary. The dash-dotted line is a straight line between the boundary points for comparison.

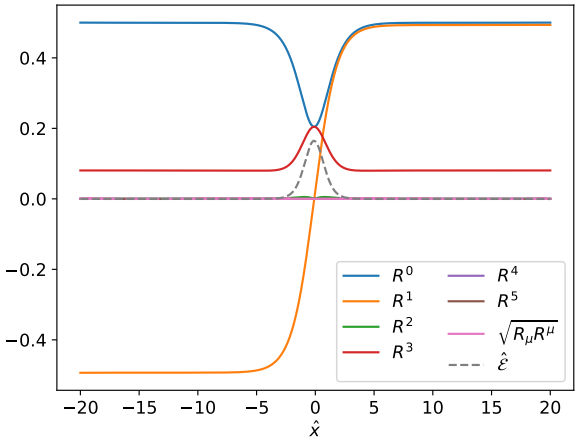

(b) R-space profiles with $\hat{G}^3(\hat{x}) = 0$ and $\theta(\hat{x}) = 0$ at the LH boundary, $\hat{G}^3(\hat{x}) = \frac{\pi}{2}$ and $\theta(\hat{x}) = \frac{\pi}{2}$ at the RH boundary.

Figure 6.7: Using gradient flow to solve for $\hat{G}^3(\hat{x})$ and $\theta(\hat{x})$, both with asymmetric boundary conditions. Charge violation is not observed, but CP-violation can be seen from the non-zero $\xi(x)$ close to the origin.

Chapter 7

Conclusion

In this thesis, we have performed numerical simulations of domain walls in the Z_2-symmetric 2HDM. We have used the gradient flow technique, which is a numerical method for finding the ground state solution in a time-independent system. We have illustrated the technique using the Goldstone model with a ϕ^4 potential as an example, where the analytical solution is known. There is a very close match between the numerical solution obtained and the analytical solution, with the energy of the numerical solution within 10^{-6} of the analytical value. We have also applied the gradient flow technique to the Z_2-symmetric 2HDM with the CP-preserving vacua and the charge-violating vacua respectively. We have introduced dimensionless quantities to simplify our gradient flow simulations. We have observed a kink solution in both the CP-preserving vacua and the charge-violating vacua.

The most general parametrization of the Higgs doublets can be obtained by performing an electroweak gauge transformation of the charge-breaking vacua. We have investigated the cases where no more than one of the $\hat{G}^a$ is non-zero in more detail. We have derived an expression for the energy density, and then the equations of motion for the vacuum parameters and the Goldstone bosons. For each of the cases, we have derived the corresponding gradient flow equations, and performed gradient flow simulations using different boundary conditions for the Goldstone bosons. In presenting our results, we have rescaled the length scale

$\hat{x} = M_h x$ and the energy scale $\hat{\mathcal{E}} = \frac{\mathcal{E}}{M_h^2 v_{\rm SM}^2}$, where M_h is the SM Higgs mass and $v_{\rm SM}$ is the VEV of the SM Higgs. We have found solutions which locally violate the neutral vacuum condition when $\hat{G}^2$ is applied with asymmetric boundary conditions. This effect can be enhanced by applying a larger relative rotation of the vacua between the boundaries. Stronger charge violation has also been observed when both θ and $\hat{G}^2$ are applied with asymmetric boundary conditions. We have also found CP-violating kink solutions for θ and $\hat{G}^3$ respectively, when asymmetric boundary conditions are imposed.

Future work could be done to implement the full system of equations that incorporate θ, $\hat{G}^1$, $\hat{G}^2$ and $\hat{G}^3$ altogether. The phenomenological implications of the non-observation of domain walls, in particular possible constraints to be imposed on the 2HDM, could also be investigated using the numerical solutions of the Z_2 domain walls.

Chapter 8

Bibliography

[1] Vilenkin, A., & Shellard, E. (1994). *Cosmic strings and other topological defects / A. Vilenkin, E.P.S. Shellard.* (Cambridge monographs on mathematical physics). Cambridge: Cambridge University Press.

[2] Kibble, T W B. (1976). Topology of cosmic domains and strings. *Journal of Physics. A, Mathematical and General, 9*(8), 1387-1398.

[3] Nielsen, H.B, & Olesen, P. (1973). Vortex-line models for dual strings. *Nuclear Physics. B, 61*, 45-61.

[4] Hooft, G.'t. (1974). Magnetic monopoles in unified gauge theories. *Nuclear Physics. B, 79*(2), 276-284.

[5] Goldstone, J. (1961). Field theories with Superconductor solutions. *Nuovo Cimento, 19*(1), 154-164.

[6] Toda, H. (1962). *Composition methods in homotopy groups of spheres* (Annals of mathematics studies ; no. 49). Princeton, N.J.: Princeton University Press.

[7] Lazanu, A, Martins, C.J.A.P, & Shellard, E.P.S. (2015). Contribution of domain wall networks to the CMB power spectrum. *Physics Letters. B, 747*(C), 426-432.

[8] Battye, Richard A, Pilaftsis, Apostolos, & Viatic, Dominic G. (2020). Domain Wall Constraints on Two Higgs Doublet Models with Z_2 Symmetry. arXiv:2010.09840 [hep-ph]

[9] Larsson, Sebastian E, Sarkar, Subir, & White, Peter L. (1997). Evading the cosmological domain wall problem. *Physical Review. D, Particles and Fields, 55*(8), 5129-5135.

[10] Bertolami, O, & Ross, G.G. (1987). Inflation as a cure for the cosmological problems of superstring models with intermediate scale breaking. *Physics Letters. B, 183*(2), 163-168.

[11] Holman, R, Kephart, T. W, & Reiss, D. B. (1988). Cosmological domain-wall problem in the $E8 \times E8$ superstring theory. *Physical Review. D, Particles and Fields, 38*(4), 1141-1143.

[12] Arnison, G et al., (1983). Experimental observation of isolated large transverse energy electrons with associated missing energy at $\sqrt{s} = 540$ GeV. *Physics Letters. B, 122*, 103-116.

[13] CDF Collaboration, F. Abe et al., (1995). "Observation of top quark production in $\overline{p}p$ collisions," *Phys. Rev. Lett. 74 2626–2631*, arXiv:hep-ex/9503002 [hep-ex].

[14] D0 Collaboration, S. Abachi et al., (1995), "Search for high mass top quark production in $p\bar{p}$ collisions at $\sqrt{s} = 1.8$ TeV," *Phys. Rev. Lett. 74* 2422–2426, arXiv:hep-ex/9411001 [hep-ex]

[15] Chatrchyan, S. et al., (2012). Observation of a new boson at a mass of 125 GeV with the CMS experiment at the LHC. *Physics Letters. B, 716*(1), 30-61.

[16] Aad, G, et al. (2012). Observation of a new particle in the search for the Standard Model Higgs boson with the ATLAS detector at the LHC. *Physics Letters. B, 716*(1), 1-29.

[17] Glashow, Sheldon L. (1961). Partial-symmetries of weak interactions. *Nuclear Physics, 22*(4), 579-588.

[18] Higgs, P.W. (1964). Broken symmetries, massless particles and gauge fields. *Physics Letters, 12*(2), 132-133.

[19] Turok, N. (1989). Global texture as the origin of cosmic structure. *Physical Review Letters, 63*(24), 2625-2628.

[20] Branco, Gustavo C, Rebelo, M.N, & Silva-Marcos, J.I. (2005). CP-odd invariants in models with several Higgs doublets. *Physics Letters. B, 614*(3-4), 187-194.

[21] Sher, M. (1989). Electroweak higgs potentials and vacuum stability. *Physics Reports, 179*(5-6), 273-418.

[22] R. G. Sachs. (1964). CP Violation in K^0 Decays. *Physical Review Letters, 13*, 286

[23] Brown, D N et al. (2004). Direct CP violating asymmetry in $B0 \to K\pi^-$ decays. *Physical Review Letters, 93*(13), 131801.1-131801.7.

[24] Chao, Y et al. (2004). Evidence for Direct CP Violation in $B^0 \to K^+\pi^-$ Decays. *Physical Review Letters, 93* 191802

[25] Observation of CP Violation in Charm Decays. (2019). *Physical Review Letters, 122*(21)

[26] Aaij, R et al. (2021). Observation of CP violation in two-body Bs0-meson decays to charged pions and kaons. *The Journal of High Energy Physics, 2021*(3)

[27] Sakharov, Andrei D. (1991). Violation of CP in variance, C asymmetry, and baryon asymmetry of the universe. *Soviet Physics. Uspekhi, 34*, 392.

[28] Branco, G.C, Ferreira, P.M, Lavoura, L, Rebelo, M.N, Sher, Marc, & Silva, João P. (2012). Theory and phenomenology of two-Higgs-doublet models. *Physics Reports, 516*(1-2), 1-102.

[29] Brawn, G. (2012). Symmetries and Topological Defects of the Two Higgs Doublet Model.

[30] Battye, Richard A, Brawn, Gary D, & Pilaftsis, Apostolos. (2011). Vacuum topology of the two Higgs doublet model. *The Journal of High Energy Physics, 2011*(8), 1-75.

[31] Battye, Richard A, Pilaftsis, Apostolos, & Viatic, Dominic G. (2021). Simulations of domain walls in Two Higgs Doublet Models. *The Journal of High Energy Physics, 2021*(1), 1-45.

[32] Lee, T.D. (1973). A theory of spontaneous T violation. *Phys. Rev., D, v. 8, No. 4, Pp. 1226-1239*

[33] Pilaftsis, Apostolos. (2012). On the classification of accidental symmetries of the two Higgs doublet model potential. *Physics Letters. B, 706*(4-5), 465-469.

[34] Djouadi, Abdelhak. (2008). The anatomy of electroweak symmetry breaking Tome II: The Higgs bosons in the Minimal Supersymmetric Model. *Physics Reports, 459*(1), 1-241.

[35] Ivanov, I. P. (2008). Minkowski space structure of the Higgs potential in the two-Higgs-doublet model. II. Minima, symmetries, and topology. *Physical Review. D, Particles, Fields, Gravitation, and Cosmology, 77*(1).

[36] Nishi, C. C. (2006). CP violation conditions in N-Higgs-doublet potentials. *Physical Review. D, Particles and Fields, 74*(3)

[37] Maniatis, M, Von Manteuffel, A, Nachtmann, O, & Nagel, F. (2006). Stability and symmetry breaking in the general two-Higgs-doublet model. *The European Physical Journal. C, Particles and Fields, 48*(3), 805-823.

[38] Aad, G et al. (2015). Combined Measurement of the Higgs Boson Mass in pp Collisions at $\sqrt{s} = 7$ and 8 TeV with the ATLAS and CMS Experiments. *Physical Review Letters, 114*